Chapter 8: Climate Models and Their Evaluation

Coordinating Lead Authors: David Randall, Richard Wood

Lead Authors: Sandrine Bony, Robert Colman, Thierry Fichefet, John Fyfe, Vladimir Kattsov, Andrew Pitman, Jagadish Shukla, Jayaraman Srinivasan, Ron Stouffer, Akimasa Sumi, Karl Taylor

Contributing Authors: K. AchutaRao (PCMDI), R. Allan (Univ. Reading), A. Berger, H. Blatter, C. Bonfils (LLNL), A. Boone, C. Bretherton (Univ. Seattle), T. Broccoli, V. Brovkin, W. Cai, M. Claussen, P. Dirmeyer (COLA), C. Doutriaux (PCMDI), H. Drange (BCCR), J.-L. Dufresne (LMD), S. Emori, A. Frei, P. Gent, P. Gleckler (PCMDI), H. Goosse, R. Graham, J. Gregory (CGAM), R. Gudgel (GFDL), A. Hall, S. Hallegatte (METEO-FRANCE), H. Hasumi, A. Henderson-Sellers, H. Hendon, K. Hodges (Univ. Reading), M. Holland (NCAR), B. Holtslag (Wageningen Univ.), E. Hunke, P. Huybrechts, W. Ingram (Oxford), F. Joos, B. Kirtmann, S. Klein (PCMDI), R. Koster (NASA), P. Kushner, J. Lanzante, M. Latif (Univ. Kiel), G. Lau, A.H. Monahan, J. Murphy (Hadley Centre), T. Osborn, T. Pavlova, V. Petoukhov, T. Phillips (PCMDI), S. Power, S. Rahmstorf, S. Raper, H. Renssen, D. Rind, M. Roberts, A. Rosati (GFDL), C. Schär (ETH), J. Scinnoca, A. Schmittner (OSU), D. Seidov, D. Smith, B. Soden (Univ. Miami), W. Stern (GFDL), K.Sudo, T.Takemura, G. Tselioudis (NASA GISS), M. Webb (Hadley Centre), M. Wild (ETH).

Review Editors: Elisa Manzini, Taroh Matsuno, Bryant McAvaney

Date of Draft: 12 August 2005

Notes: This is the TSU compiled version

Figures

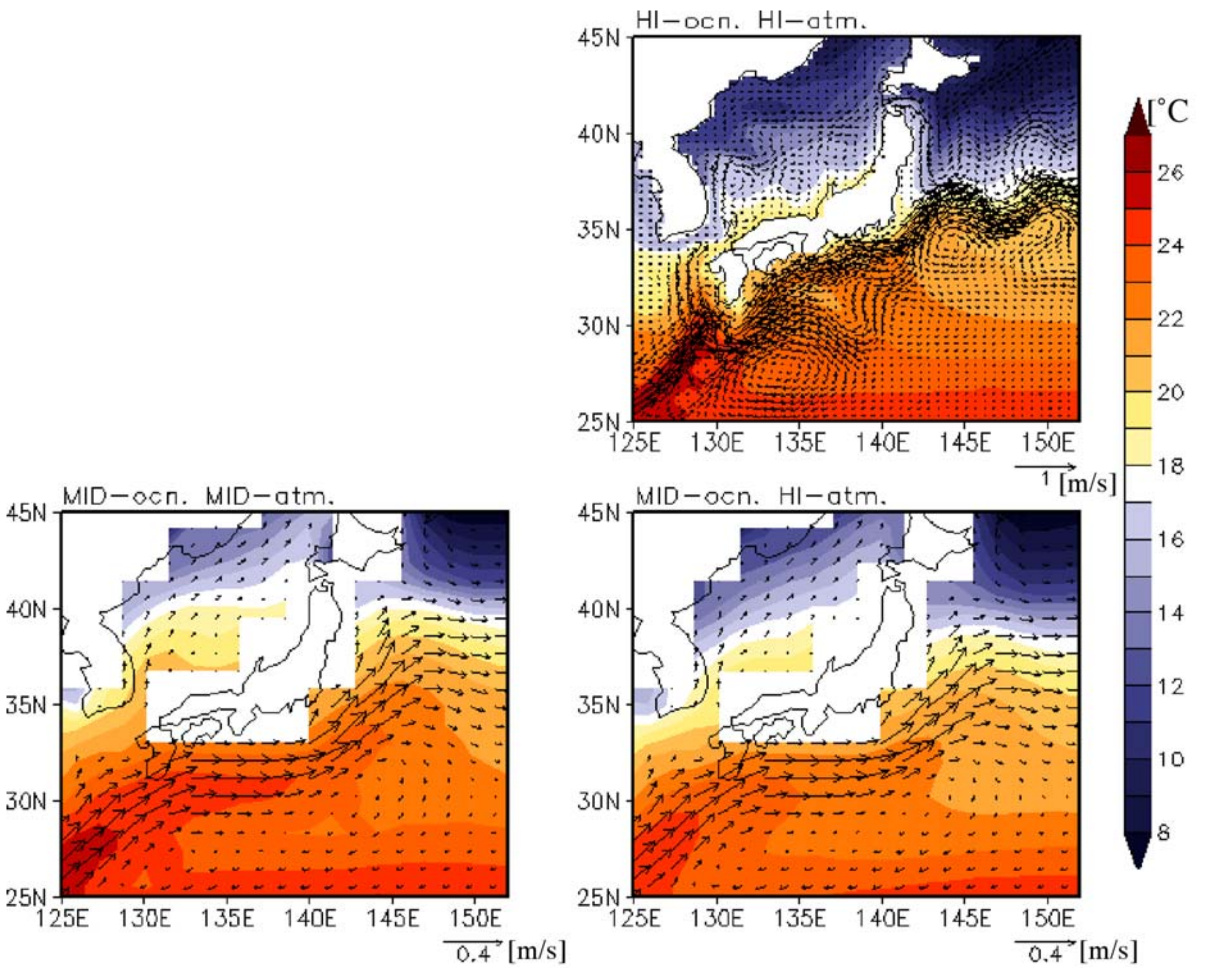

Figure 8.2.1. Long--term mean Sea surface temperature (°C) and ocean current velocities at 100-m depth(vectors, unit: m s^{-1}) around the Kuroshio and the Kuroshio Extension, simulated by MIROC-hi ("HI-ocn. HI-atm") and MIROC-mid ("MID-ocn. MID-atm") in the control experiment forced by pre-industrial conditions (control-run; averaged for 100 years). Also shown is the result from a model with the atmospheric resolution of MIROC-hi but the ocan resolution of MIROC-mid ("MID-ocn HI-atm"). More structure in the temperature and velocity fields is captured on scales of of a few degree lat/long with the high resolution ocean, even though the mid-resolution ocean could be argued to (marginally) resolve these scales.

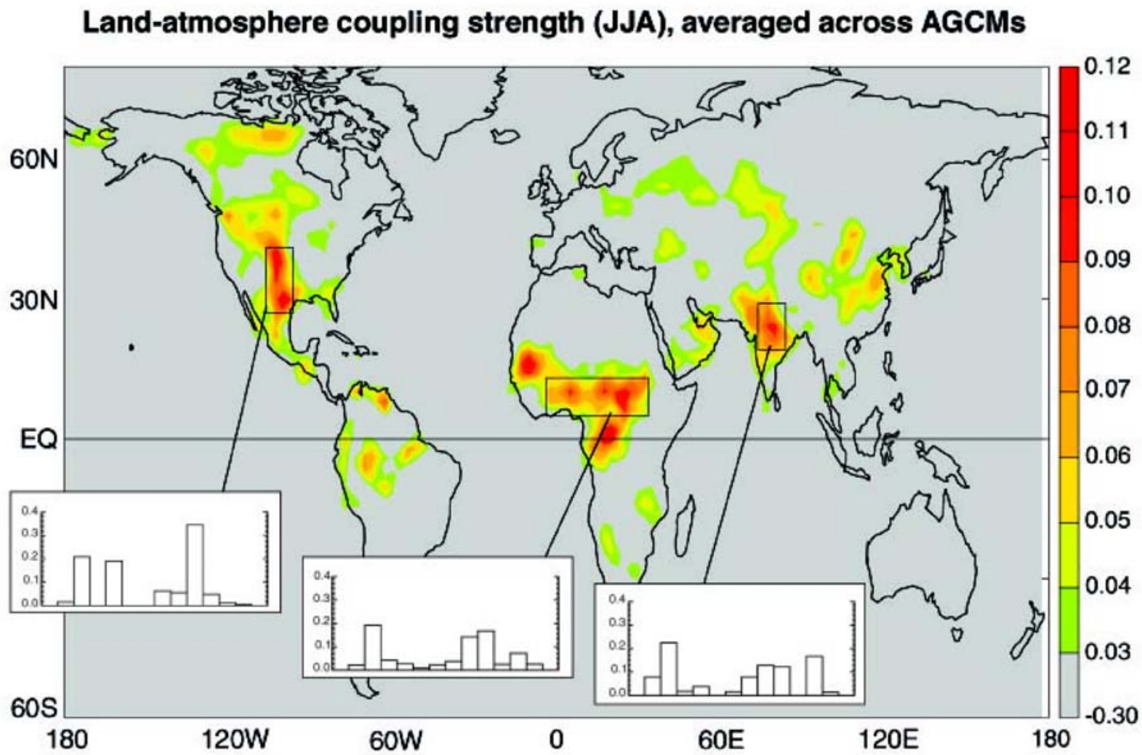

Figure 8.2.2. The land-atmosphere coupling strength diagnostic for boreal summer (the difference, dimensionless, describing the impact of soil moisture on precipitation), averaged across the 12 models participating in GLACE. (**Insets**) Areally averaged coupling strengths for the 12 individual models over the outlined, representative hotspot regions. No signal appears in southern South America or at the southern tip of Africa.

(a)

(b)

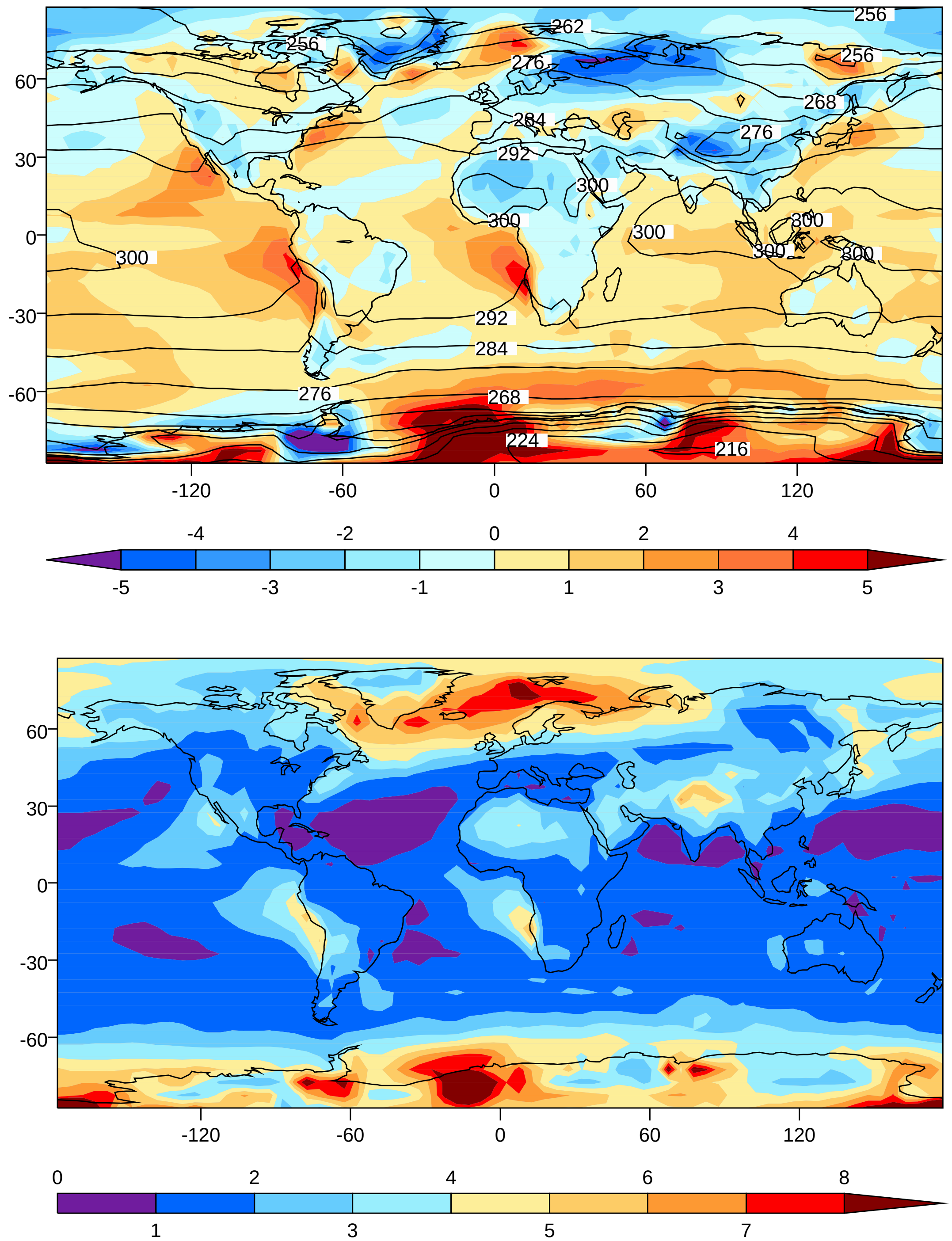

Figure 8.3.1. Observed climatological annual-mean sea surface temperature (SST) and, over land, surface air temperature (labeled contours in panel a) and the multi-model mean error in these temperatures, simulated minus observed (color-shaded contours in panel a); also root-mean-square model error in this temperature, based on all available IPCC model simulations (panel b). The observations are from the CRU merged SST and surface air temperature dataset for the period 1961–1990 (Jones, 1999), and the model results are from years 1980–1999 of the CMIP 20th Century simulations. Temperature units are degrees kelvin (K).

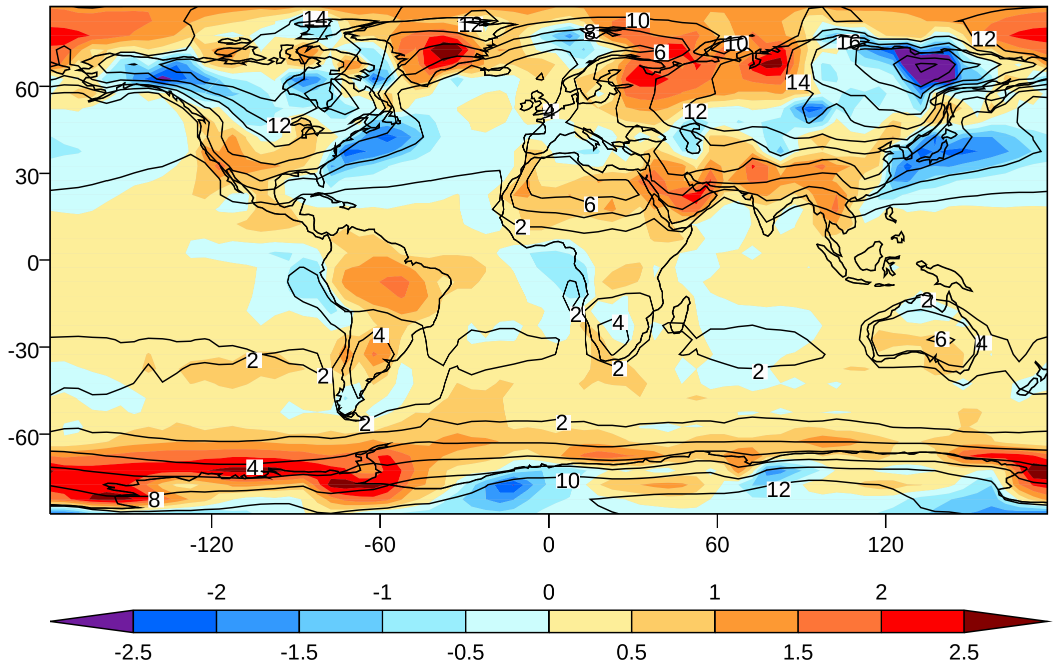

Figure 8.3.2. Observed standard deviation (labeled contours) of sea surface temperature (SST) and, over land, surface air temperature, computed over the climatological monthly mean annual cycle, and the multi-model mean error in these temperatures, simulated minus observed (color-shaded contours). The observations are from the CRU merged SST and surface air temperature dataset for the period 1961–1990 (Jones, 1999), and the model results are from years 1980–1999 of the CMIP 20th Century simulations. Temperature units are degrees kelvin (K).

'

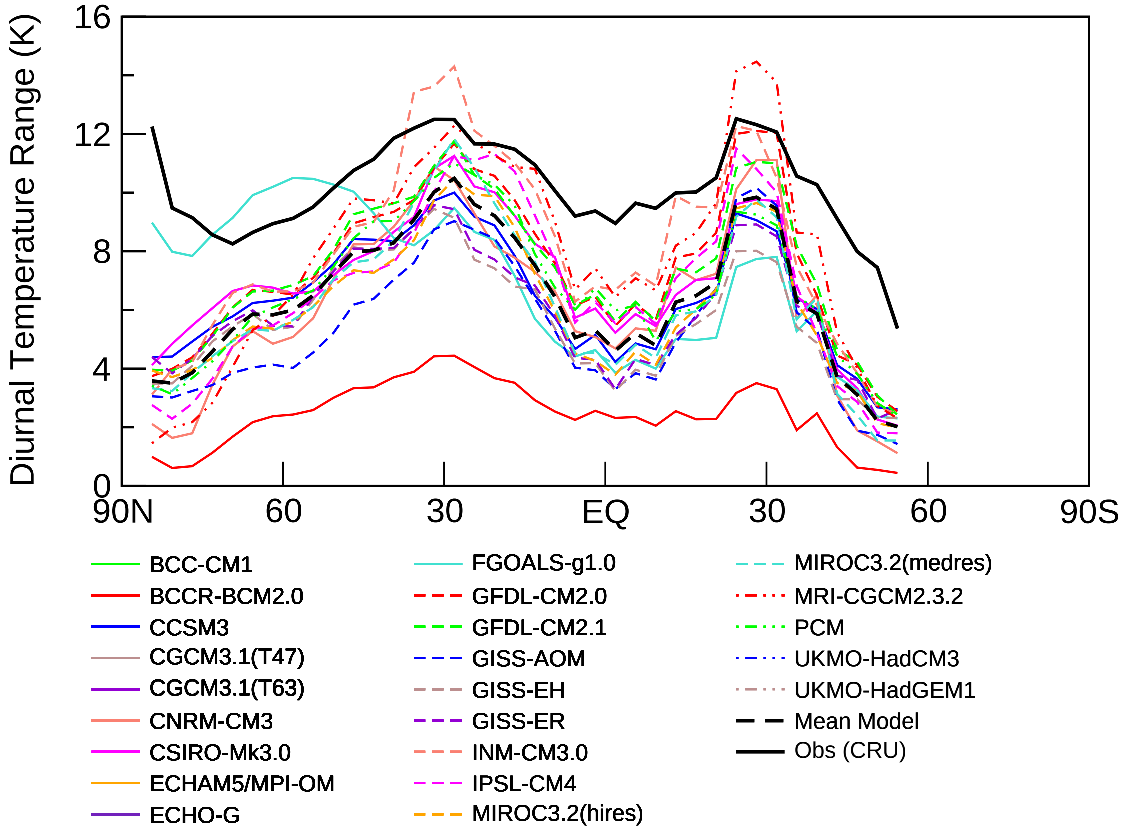

Figure 8.3.3. Diurnal range of surface air temperature, averaged zonally over land areas and averaged annually. The observations are from the CRU surface air temperature dataset for the period 1961–1990 (New et al., 1999), and the model results are from years 1980–1999 of the CMIP 20th Century simulations. Results are not shown where observations are sparse (e.g., Antarctica).

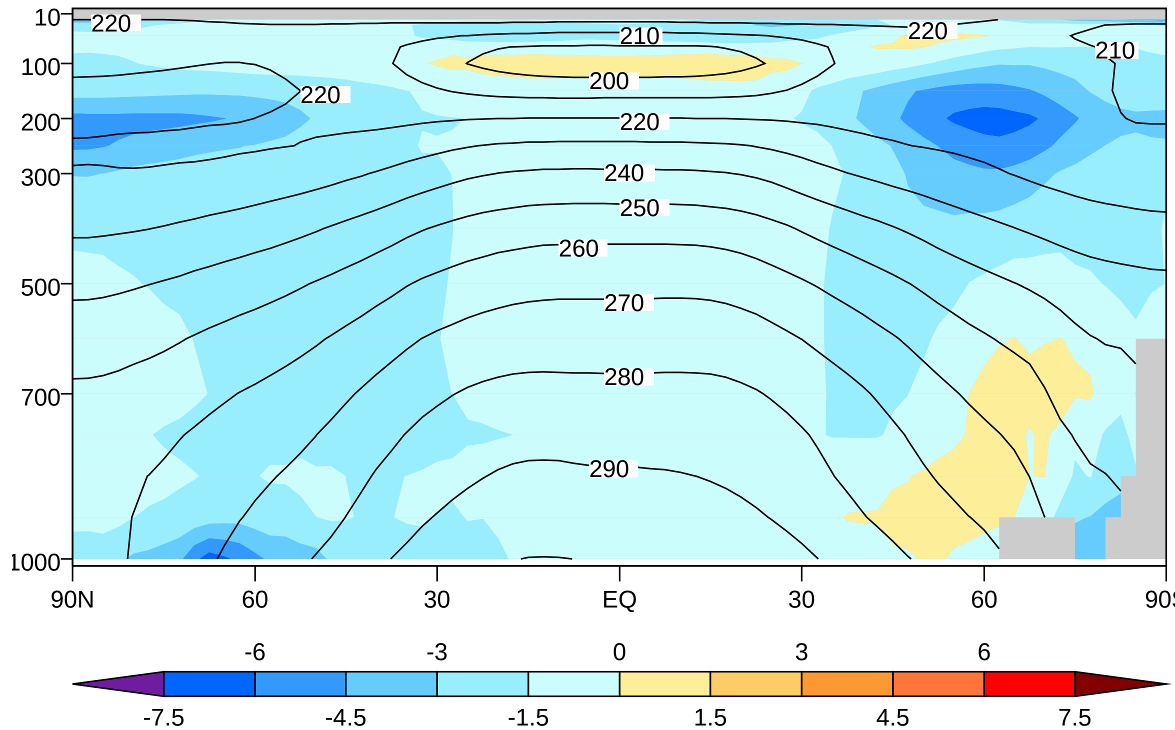

Figure 8.3.4. Observed climatological annual-mean air temperature (K), averaged zonally (labeled contours), and the multi-model mean error in this field, simulated minus observed (color-filled contours). The observational estimate is from the 40-year European Reanalysis (ERA40, Uppala et al., 2005) based on observations over the period 1980–1999. The model results are from the same period of the CMIP 20th Century simulations.

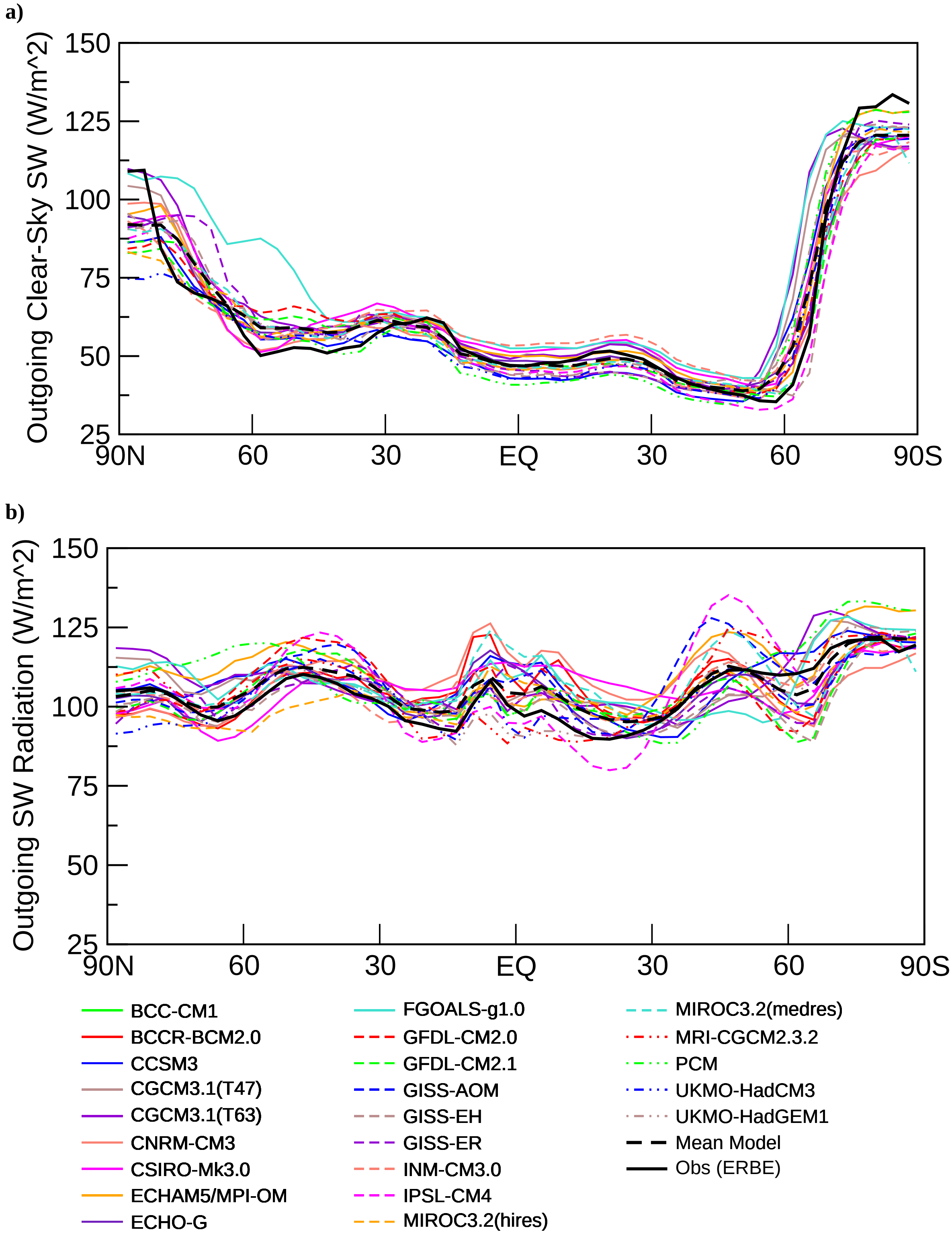

Figure 8.3.5. Annual-mean, zonally-averaged shortwave radiation scattered and reflected to space under clear-sky conditions (panel a) and under "all-sky" conditions (both clear and cloudy, panel b). The observational estimates are from radiometers flown on satellites during the period 1985–1989 (ERBE, Barkstrom et al., 1989). The model results are from years 1980–1999 of the CMIP 20th Century simulations.

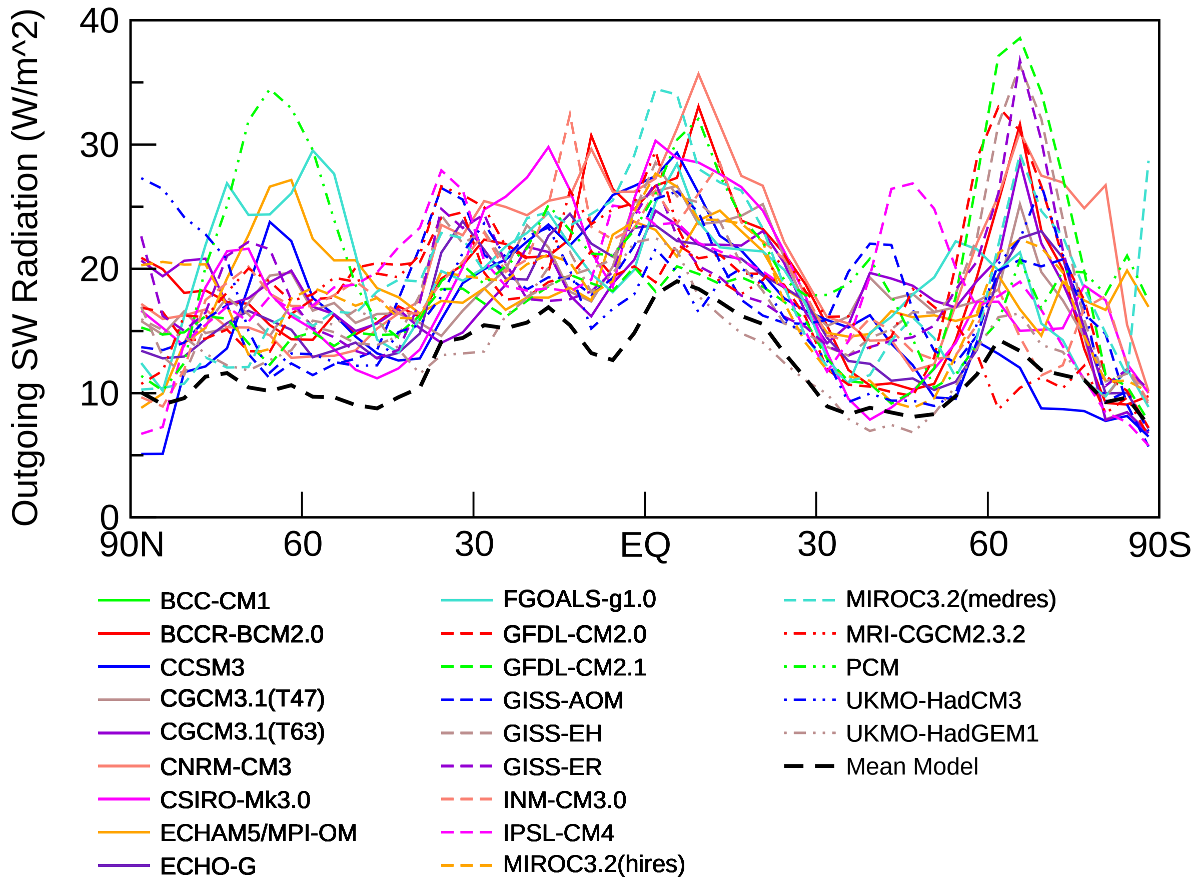

Figure 8.3.6. Root-mean-square (RMS) model error, as a function of latitude, in simulation of outgoing shortwave radiation scattered and reflected to .space. The RMS error is calculated over all longitudes and over all months. The mean model result is computed by first calculating the multi-model monthly mean fields, and then calculating the RMS error (i.e., it is *not* the mean of the individual model results). The observational estimates are from radiometers carried by satellites during the period 1985–1989 (ERBE, Barkstrom et al., 1989). The model results are from years 1980–1999 of the CMIP 20th Century simulations.

(a)

(b)

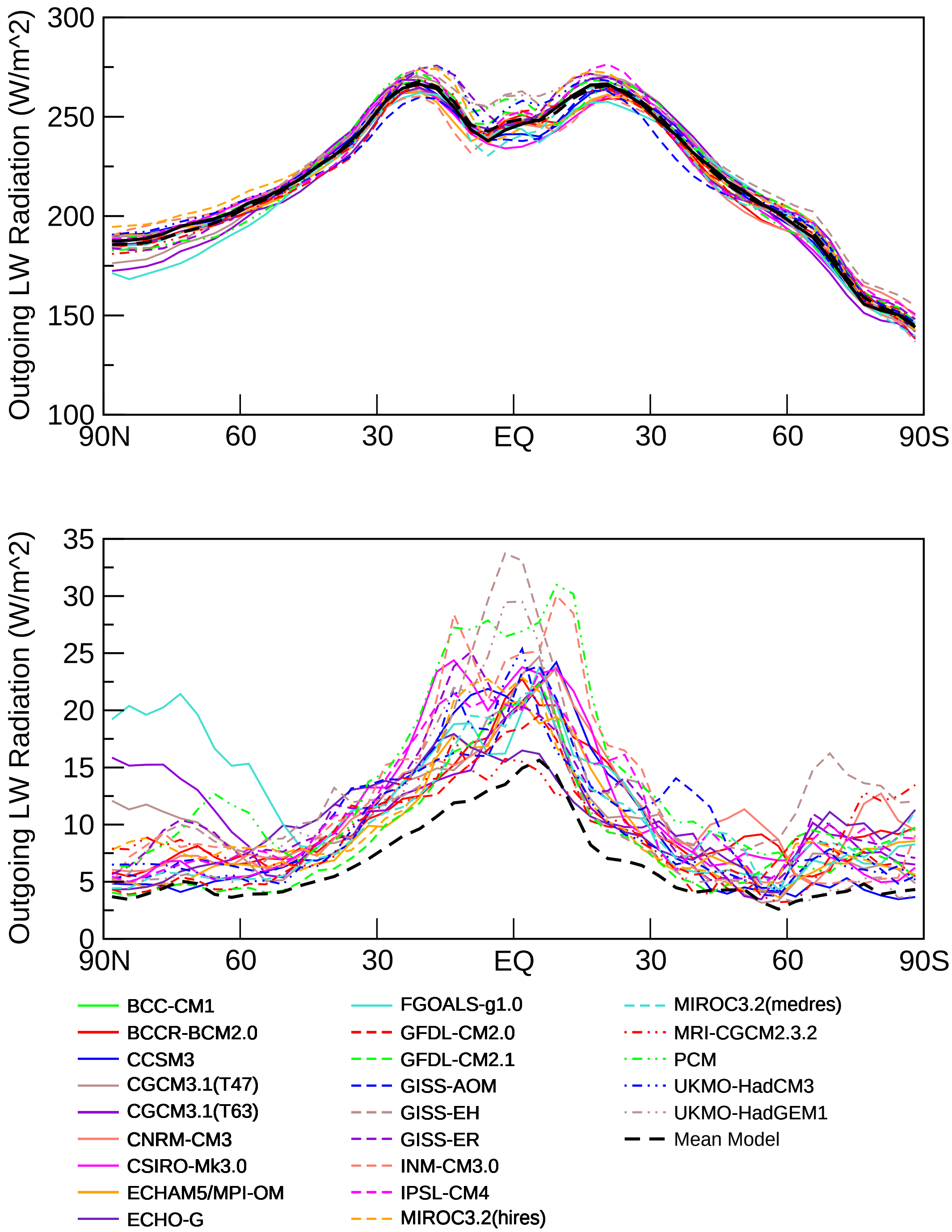

Figure 8.3.7. Annual-mean, zonally-averaged outgoing longwave radiation at the top of the atmosphere (panel a), and root-mean-square (RMS) model error, as a function of latitude (panel b). The RMS error is calculated over all longitudes and over all months. The mean model result is computed by first calculating the multi-model monthly mean fields, and then calculating the RMS error (i.e., it is *not* the mean of the individual model results). The observational estimates are from radiometers flown on satellites during the period 1985–1989 (ERBE, Barkstrom et al., 1989), and the model results are from years 1980–1999 of the CMIP 20th Century simulations.

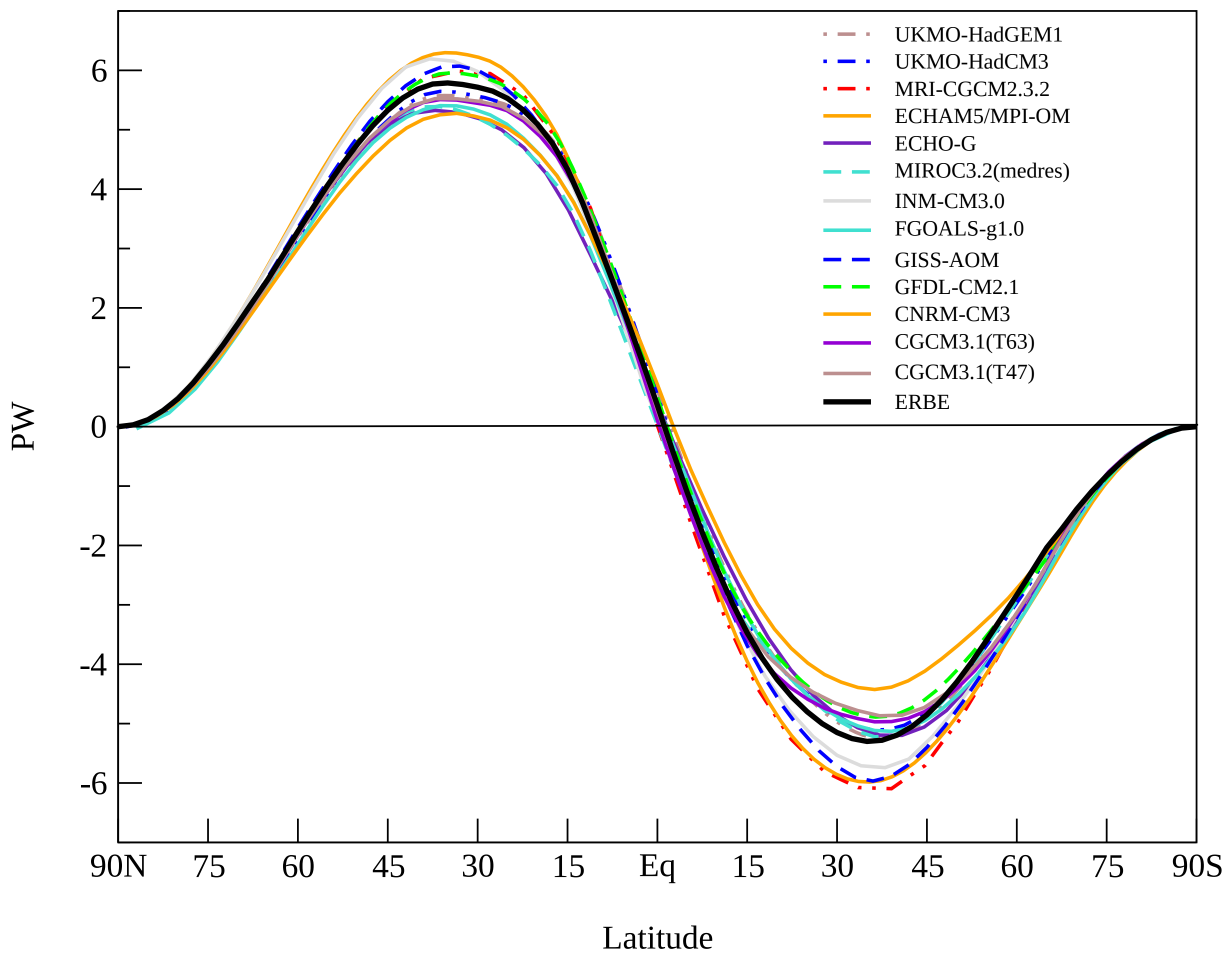

Figure 8.3.8. Total energy transport by the oceans and the atmosphere, averaged zonally and over time, as implied by the net flux of radiation at the top of the atmosphere. The observational estimates are from radiometers flown on satellites during the period 1985–1989 (ERBE, Barkstrom et al., 1989). The model results are from years 1980–1999 of climate of the CMIP 20th Century simulations.

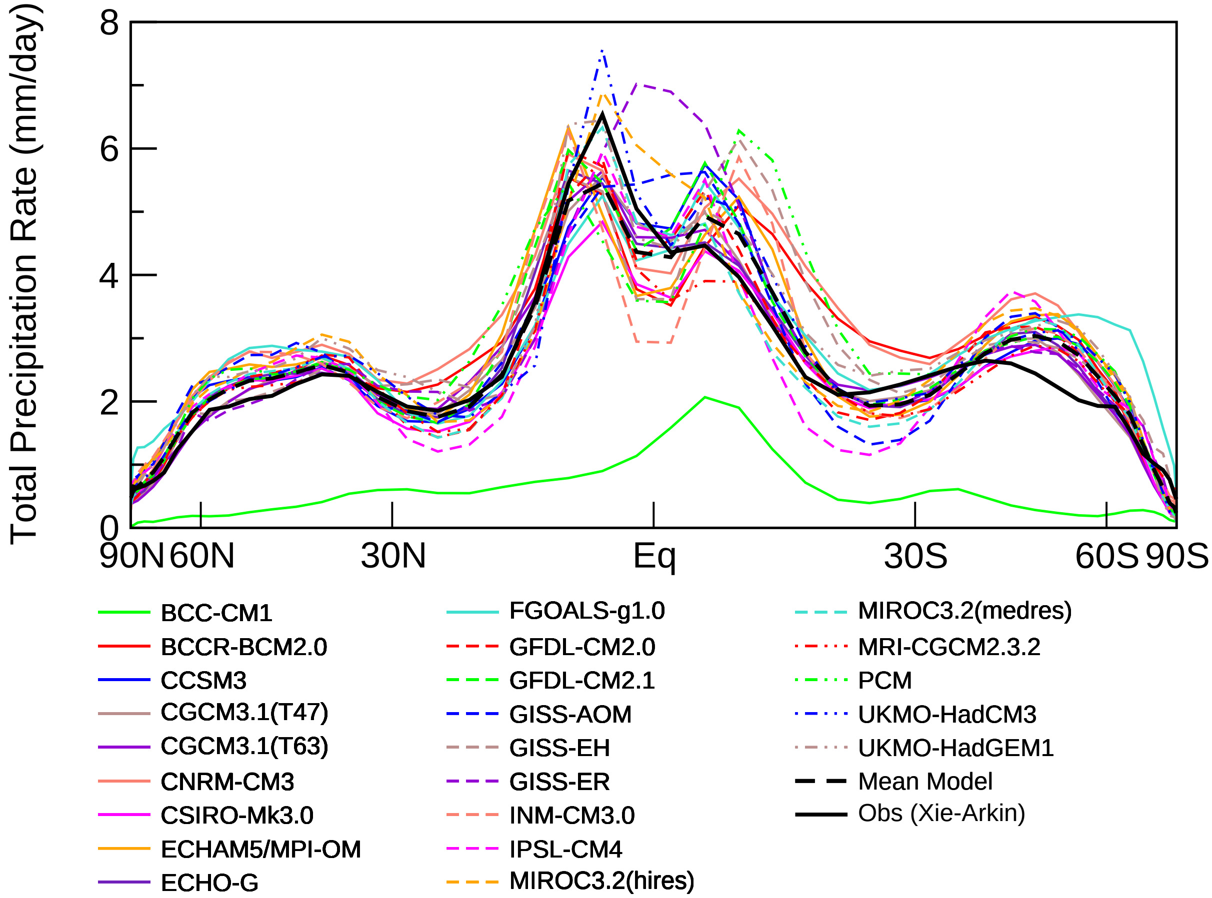

Figure 8.3.9. Time-mean of the zonally-averaged precipitation rate. The observational estimates are from Xie and Arkin (1997) for the period 1979–1993, and the model results are from years 1980–1999 of the CMIP 20th Century simulations.

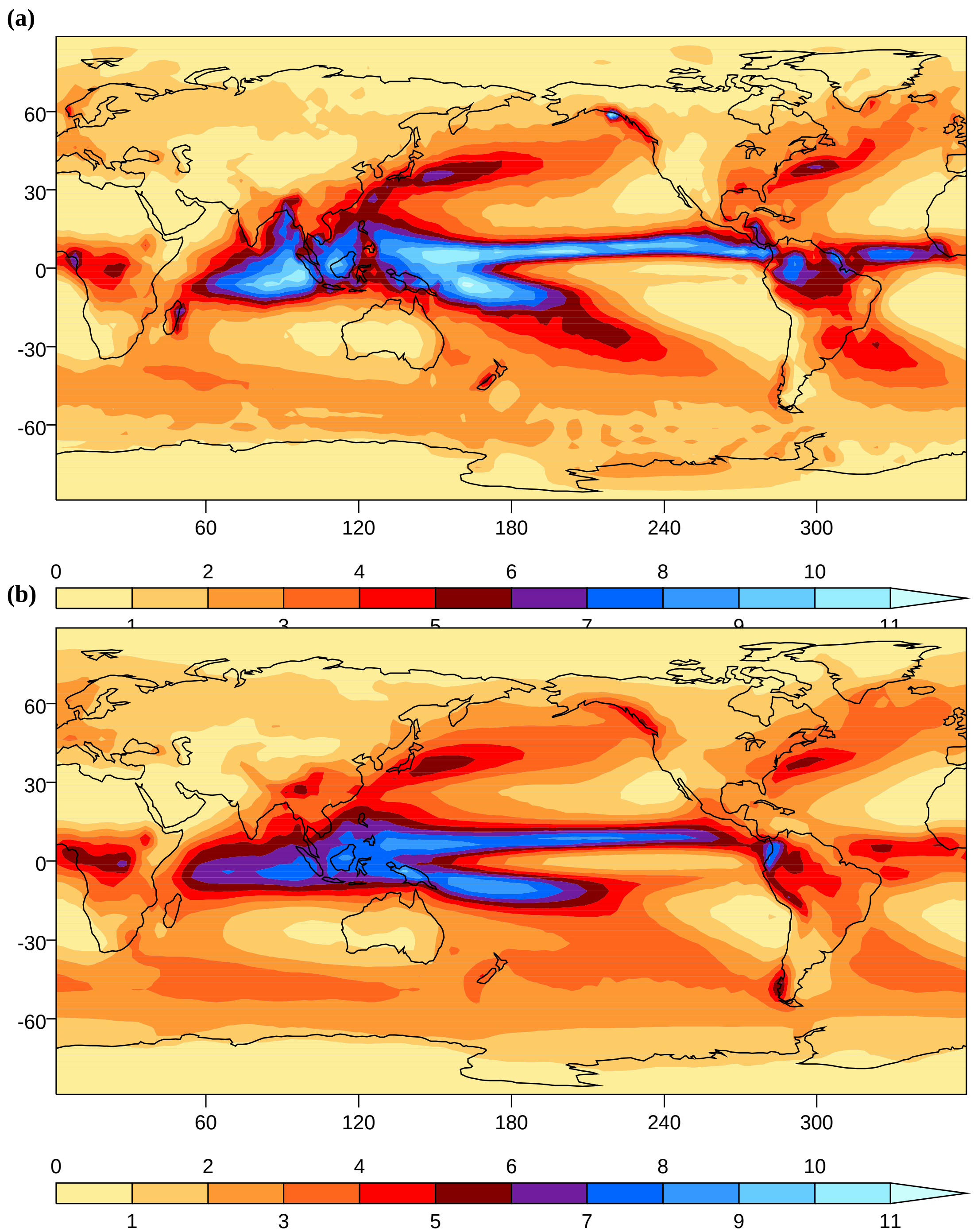

Figure 8.3.10. Annual-mean precipitation rate (mm/day), observed (panel a) and model simulated (panel b). The observational estimates are from Xie and Arkin (1997) for the period 1979–1993, and the model results are from years 19801999 of the CMIP 20th Century simulations.

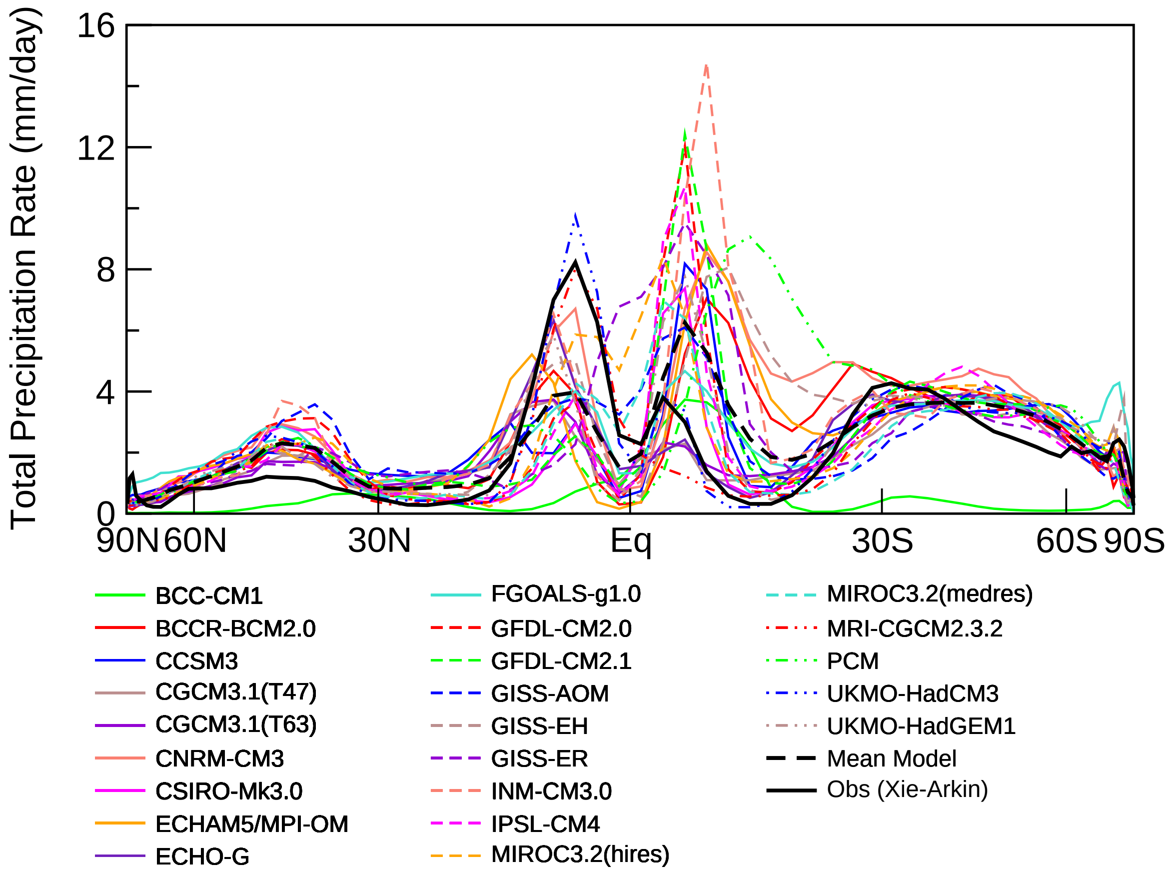

Figure 8.3.11. Observed and model simulated precipitation rate in the eastern Pacific averaged over a sector from 120°W to 100°W and averaged over the months of March, April, and May. The observational estimates are from Xie and Arkin (1997) for the period 1979–1993, and the model results are from years 1980–1999 of the CMIP 20th Century simulations.

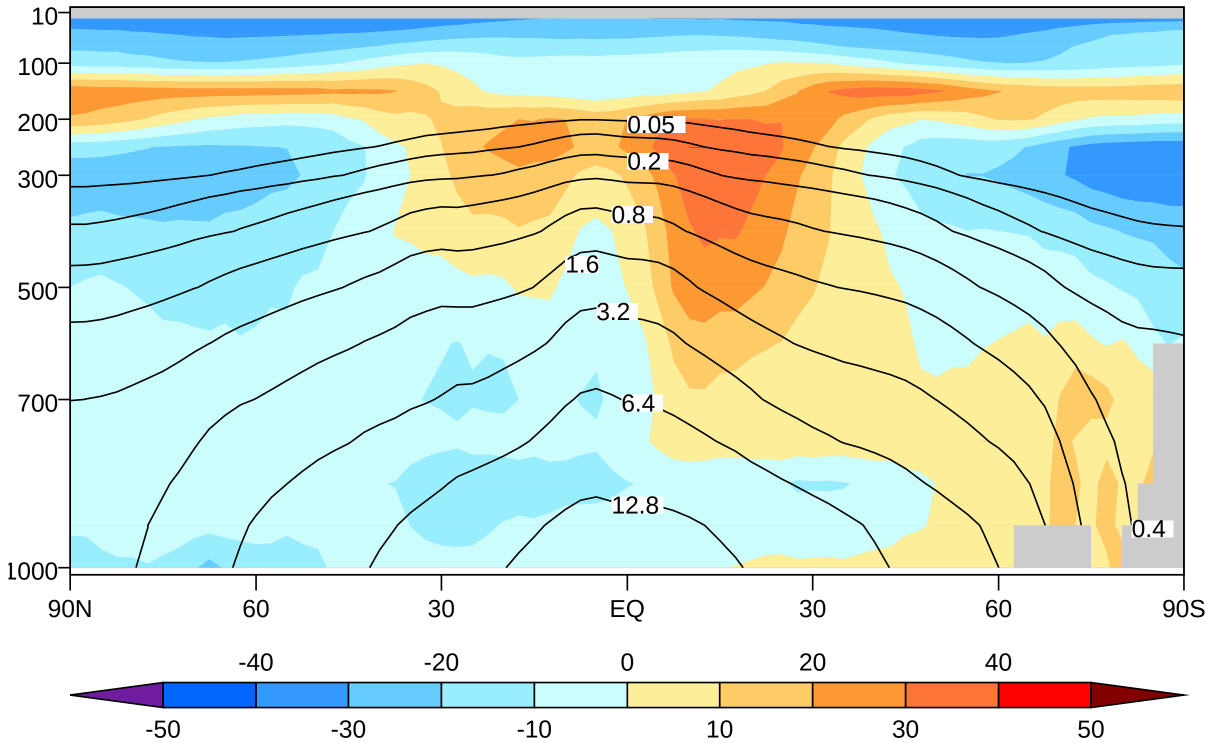

Figure 8.3.12. Observed specific humidity (g/kg), averaged zonally and annually (labeled contours), and the multi-model mean fractional error in this field, simulated minus observed, divided by observed (color-filled contours). The observational estimate is from the 40-year European Reanalysis (ERA40, Uppala et al., 2005) based on observations over the period 1980–1999. The model results are from the same period of the CMIP 20th Century simulations.

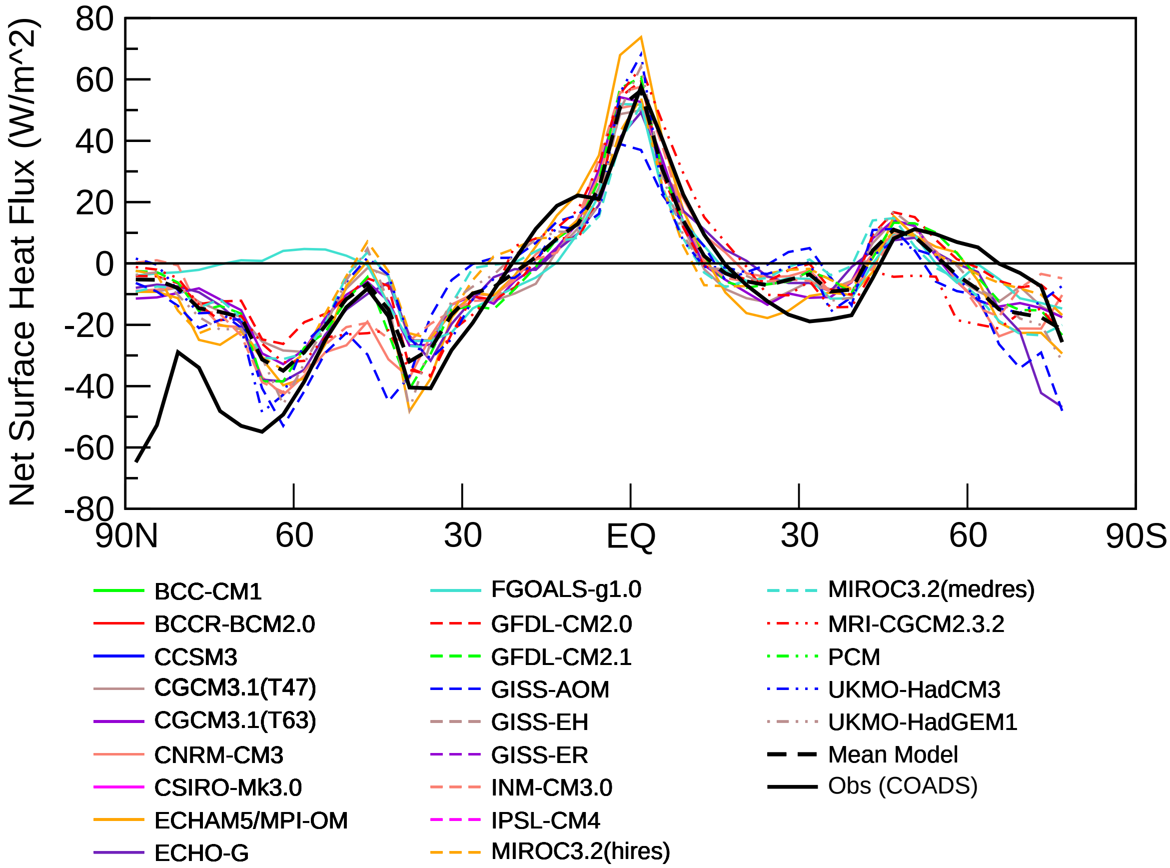

Figure 8.3.13. Annual mean, zonally averaged, total surface heat flux into the oceans. The observational estimates are from da Silva (1994), and are based on COADS observations over the period 1945–1989. The model results are from years 1980–1999 of the CMIP 20th Century simulations.

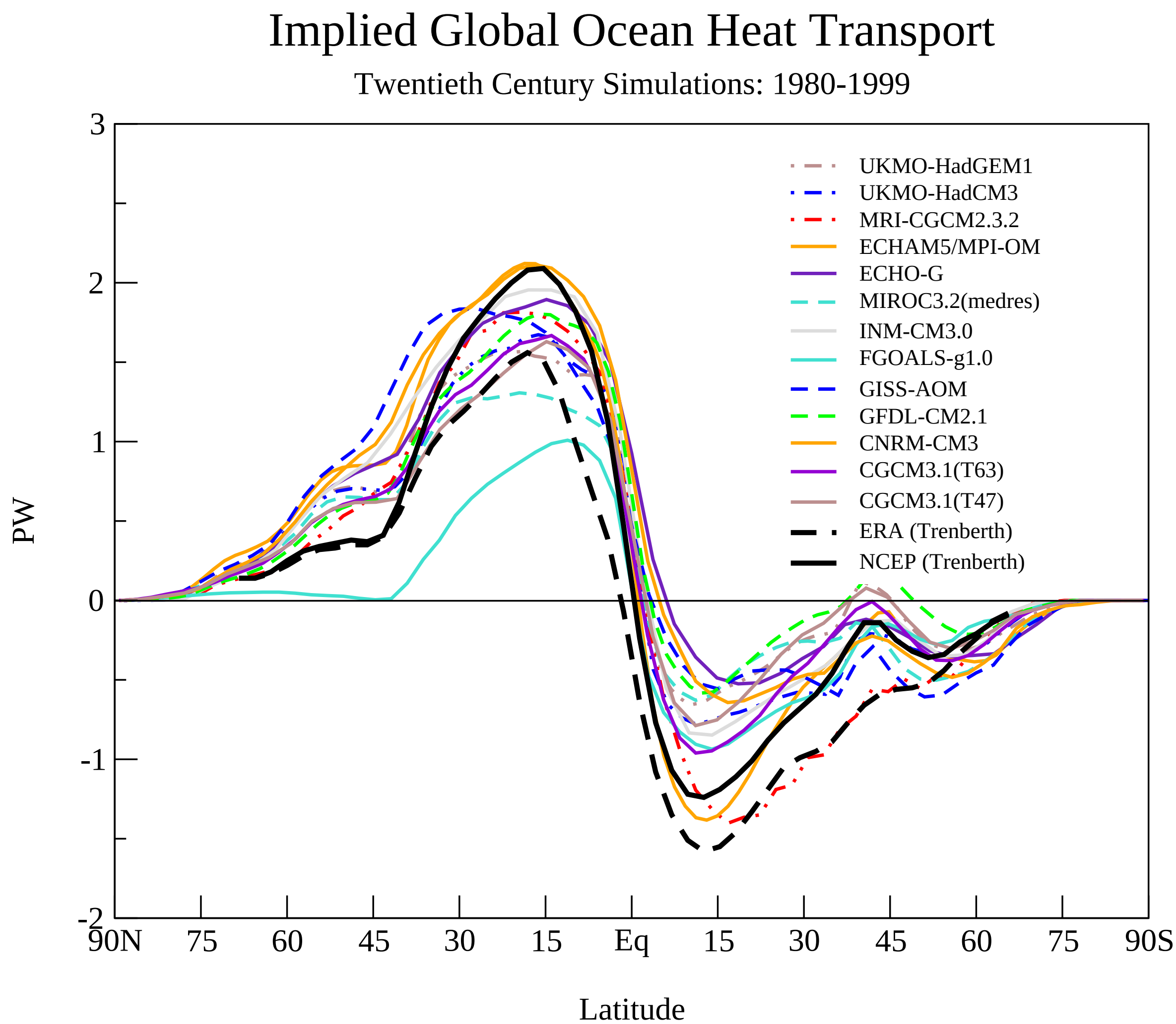

Figure 8.3.14. Annual mean, zonally averaged implied oceanic heat transport. The observational estimates are from NCEP and ERA40 reanalyses.The model results are from years 1980–1999 of the CMIP 20th Century simulations.

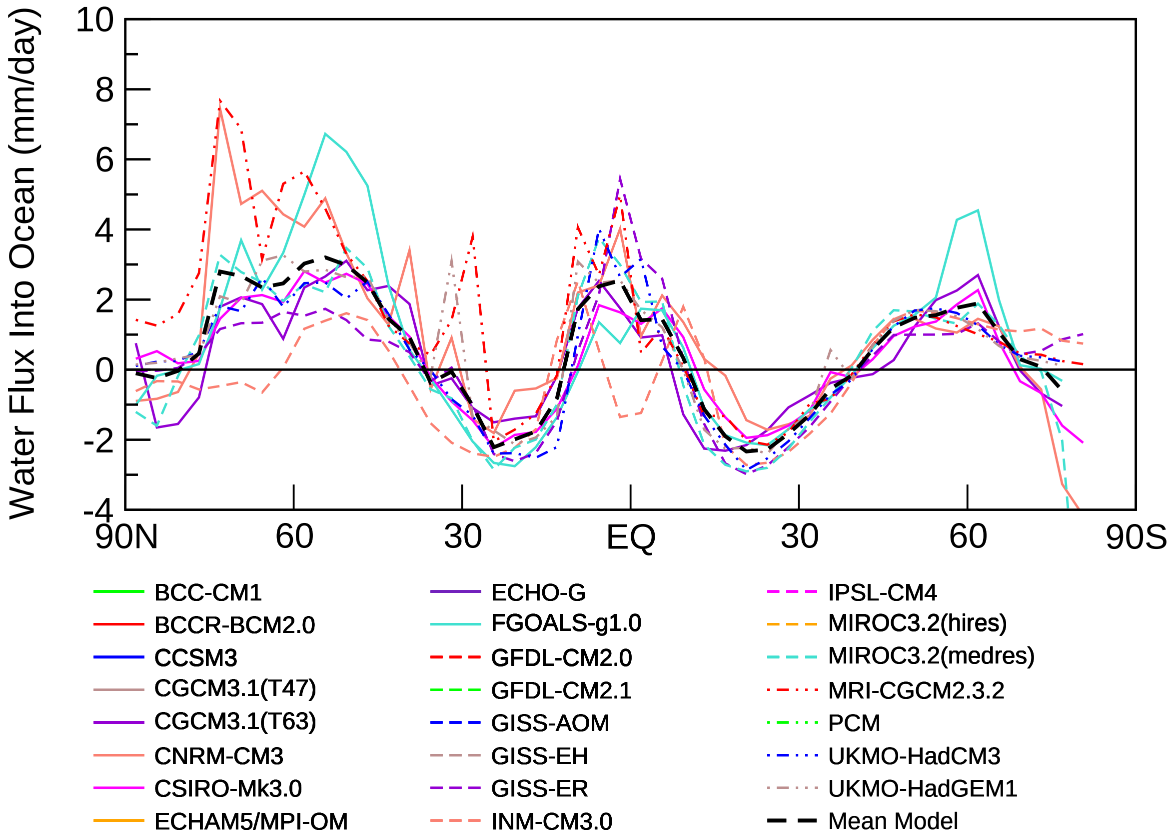

Figure 8.3.15. Annual mean net rate of fresh water added to the ocean from: 1) the atmosphere (i.e., precipitation minus evaporation), 2) runoff at continental margins, and 3) any net flux due to imbalances in the freezing and melting of sea ice. Land areas are ignored in computing the zonal means. Model results are from years 1980–1999 of the CMIP 20th Century simulations.

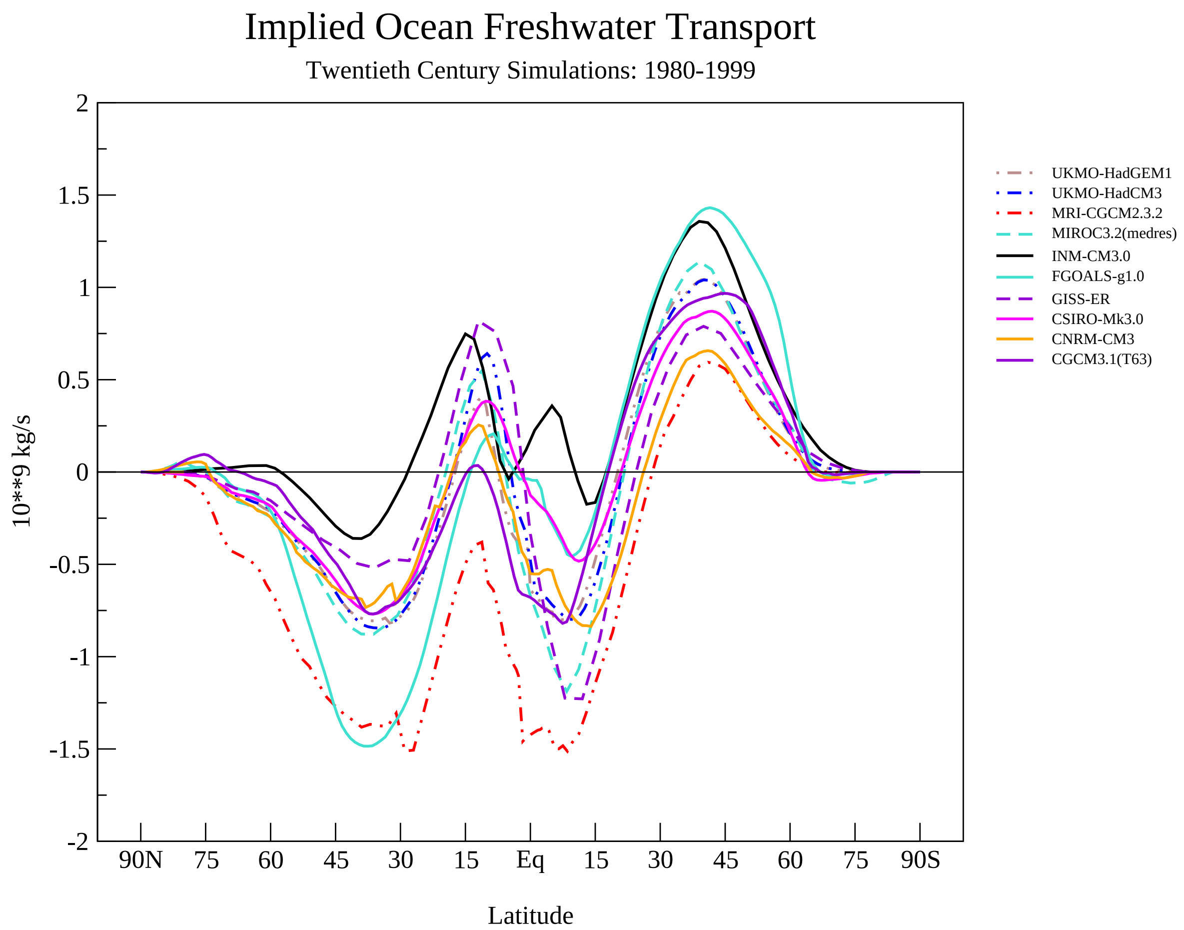

Figure 8.3.16. Annual mean, zonally averaged implied fresh water transport by the world's oceans. The model results are from years 1980–1999 of the CMIP 20th Century simulations.

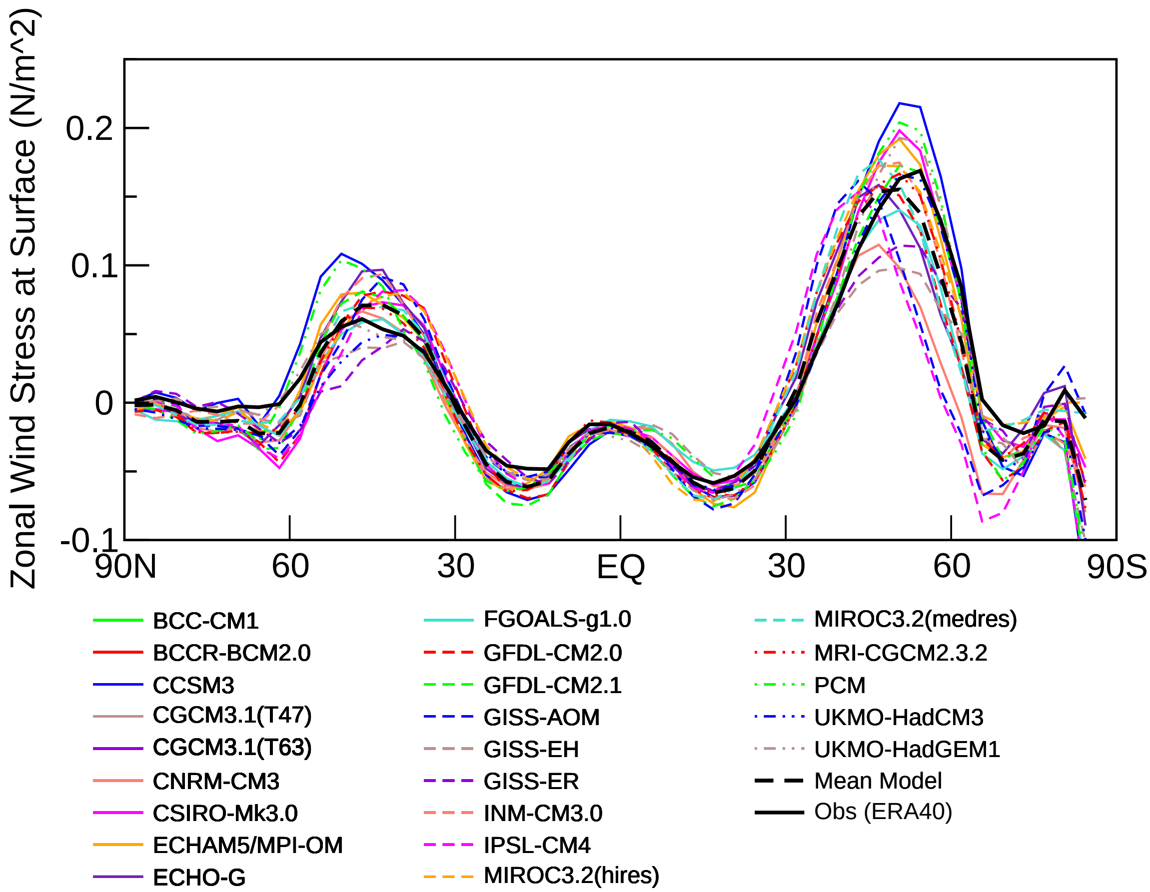

Figure 8.3.17. Surface zonal wind stress, annually and zonally averaged over the oceans. The observationally-based estimates are from the 40-year European Reanalysis (ERA40, Uppala et al., 2005) for the period 1960–2000.The model results are from years 1980–1999 of climate of the CMIP 20th Century simulations.

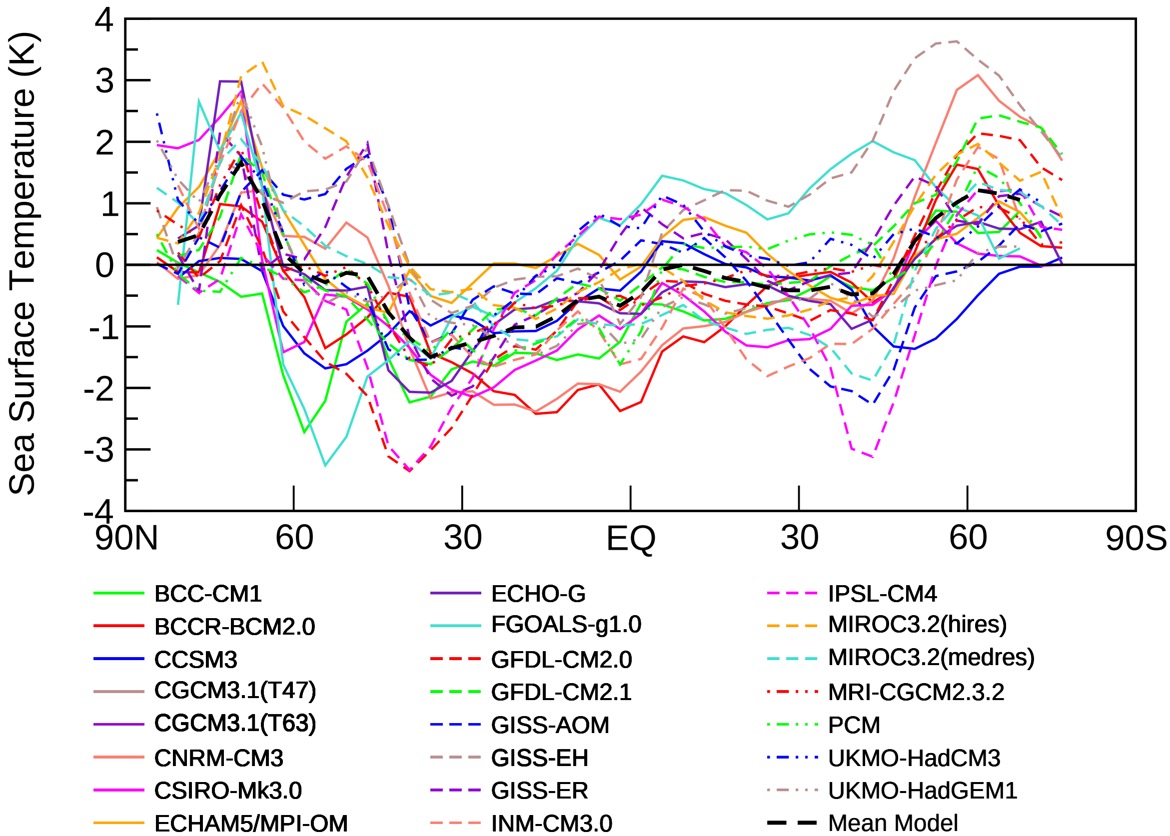

Figure 8.3.18. Zonally averaged, time mean sea surface temperature (SST) error, simulated minus observed. The observations are from the HadISST data sets for the period 1980–1999 (Rayner et al. 2003), and the model results are from years 1980–1999 of climate of the CMIP 20th Century simulations.

(a)

(b)

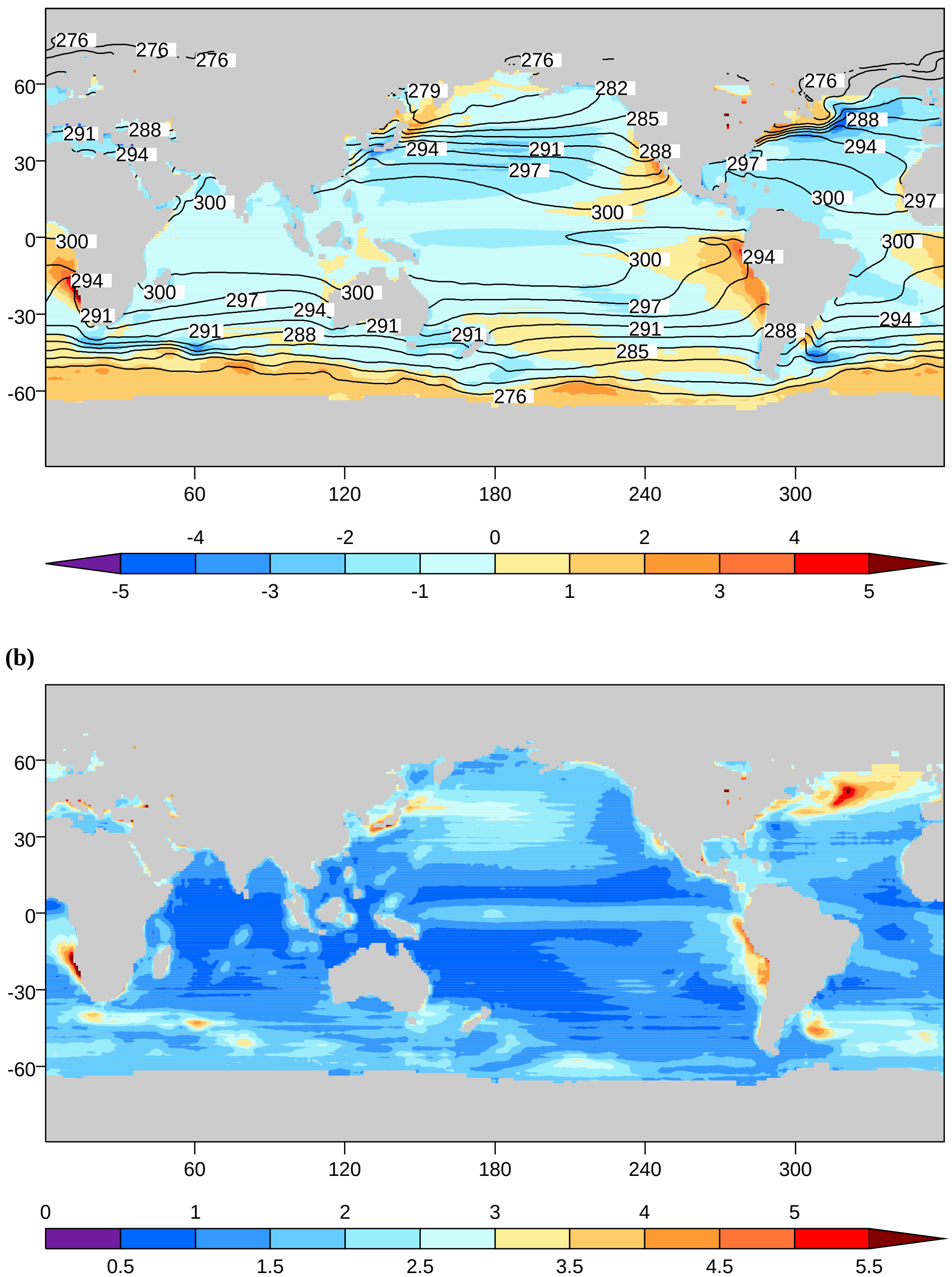

Figure 8.3.19. Observed sea surface temperature (labeled contours, panel a), multi-model mean SST error, simulated minus observed (color-filled contours, panel a), and the root-mean-squared SST error, computed over all models (panel b). Regions with sea ice have been masked because SST is unavailable from most models in these regions. The observations are from the HadISST SST data set for the period 1961–1990 (Rayner et al. 2003), and model results are from years 1980–1999 of the CMIP 20th Century simulations. Temperature units are Kelvin (K).

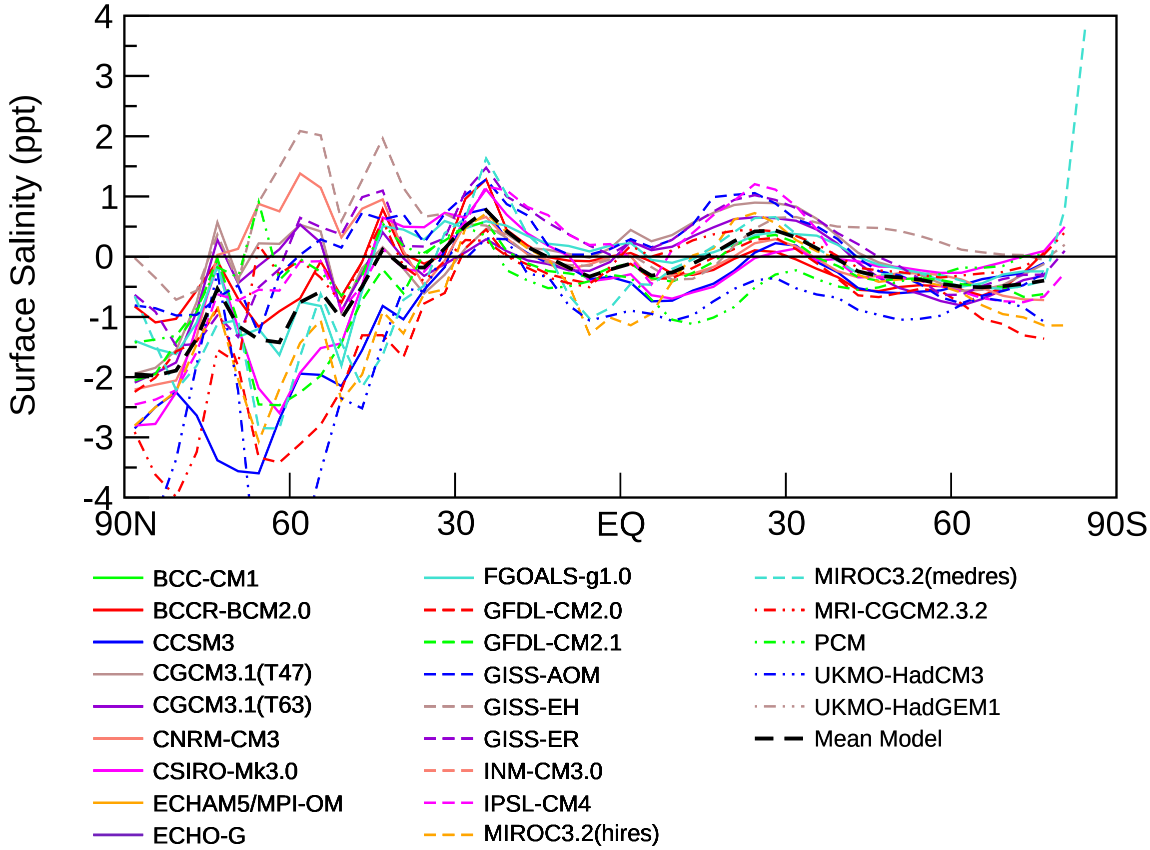

Figure 8.3.20. Annual mean, zonally averaged, sea surface salinity error (PSU???), simulated minus observed. The observations are from the 2004 World Ocean Atlas (WOA-2004) compiled by Levitus et al. (2005), and model results are from years 1950–1999 of the CMIP 20th Century simulations.

(a)

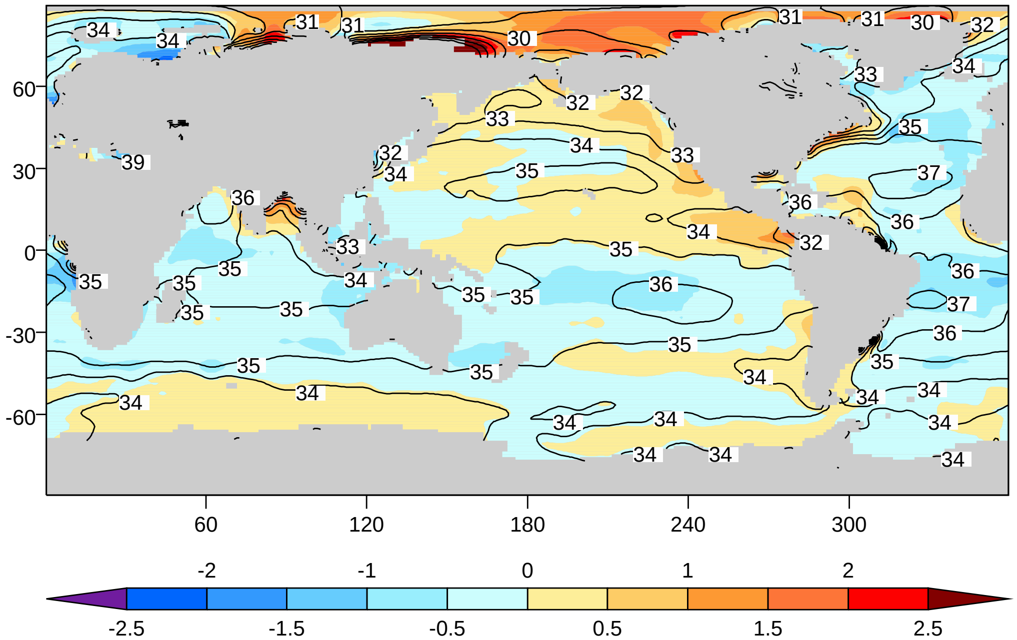

(b)

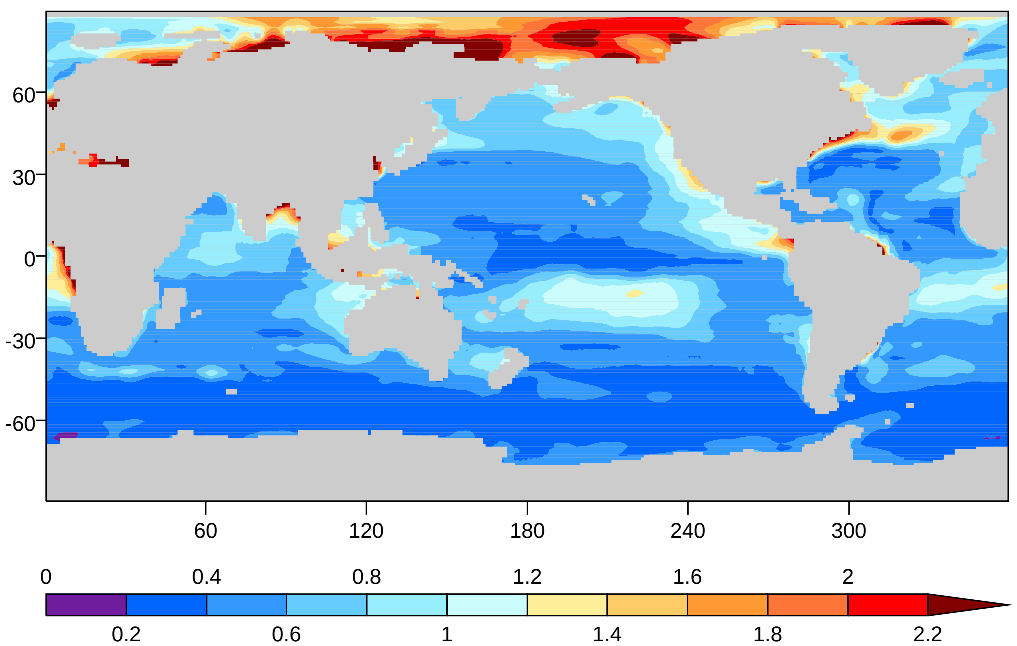

Figure 8.3.21. Observed surface salinity (psu, labeled contours, panel a), multi-model mean surface salinity error, simulated minus observed (color-filled contours, panel a), and the root-mean-squared surface salinity error, computed over all models (panel b). The observations are from the 2004 World Ocean Atlas (WOA-2004) compiled by Levitus et al. (2005), and model results are from years 1950–1999 of climate of the CMIP 20th Century simulations.

(a)

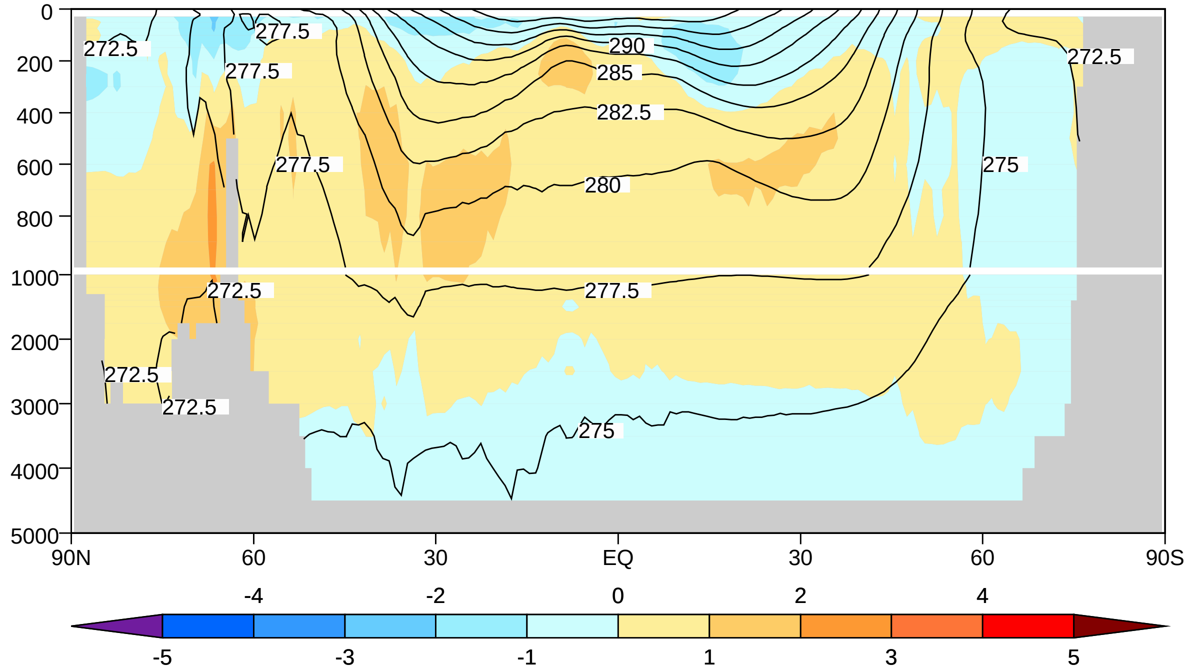

(b)

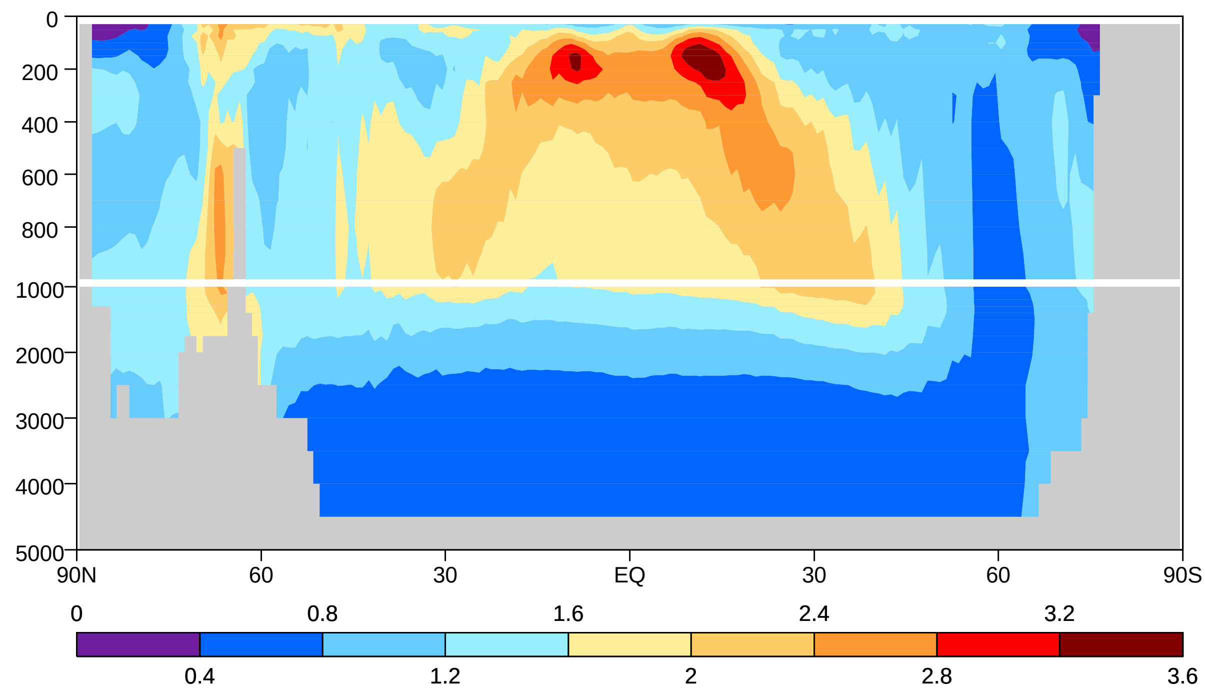

Figure 8.3.22. Observed climatological annual-mean potential temperature, zonally averaged over all ocean basins (panel a, labeled contours), multi-model mean error in this field, simulated minus observed (color-filled contours, panel a), and the root-mean-squared error in this field, computed over all models (panel b). The observations are from the 2004 World Ocean Atlas (WOA-2004) compiled by Levitus et al. (2005), and model results are from years 1950–1999 of the CMIP 20th Century simulations. Temperature units are Kelvin (K).

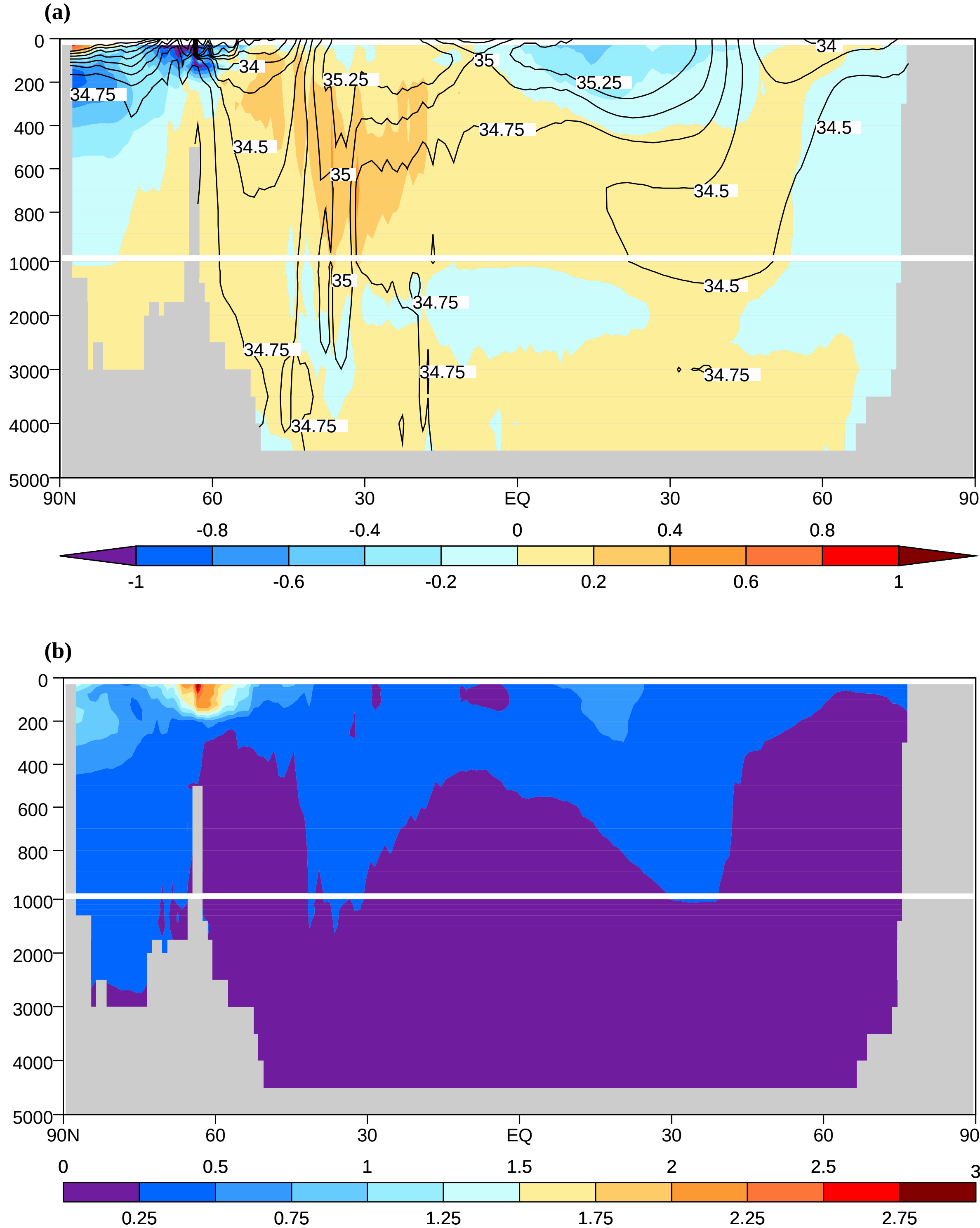

Figure 8.3.23. Observed climatological annual-mean salinity, zonally averaged over all ocean basins but excluding isolated inland seas and lakes (labeled contours, panel a), multi-model mean error in this field, simulated minus observed (color-filled contours, panel a), and the root-mean-squared error in this field, computed over all models (panel b). The observations are from the 2004 World Ocean Atlas (WOA-2004) compiled by Levitus et al. (2005), and model results are from years 1950–1999 of the CMIP 20th Century simulations. Salinity units are psu.

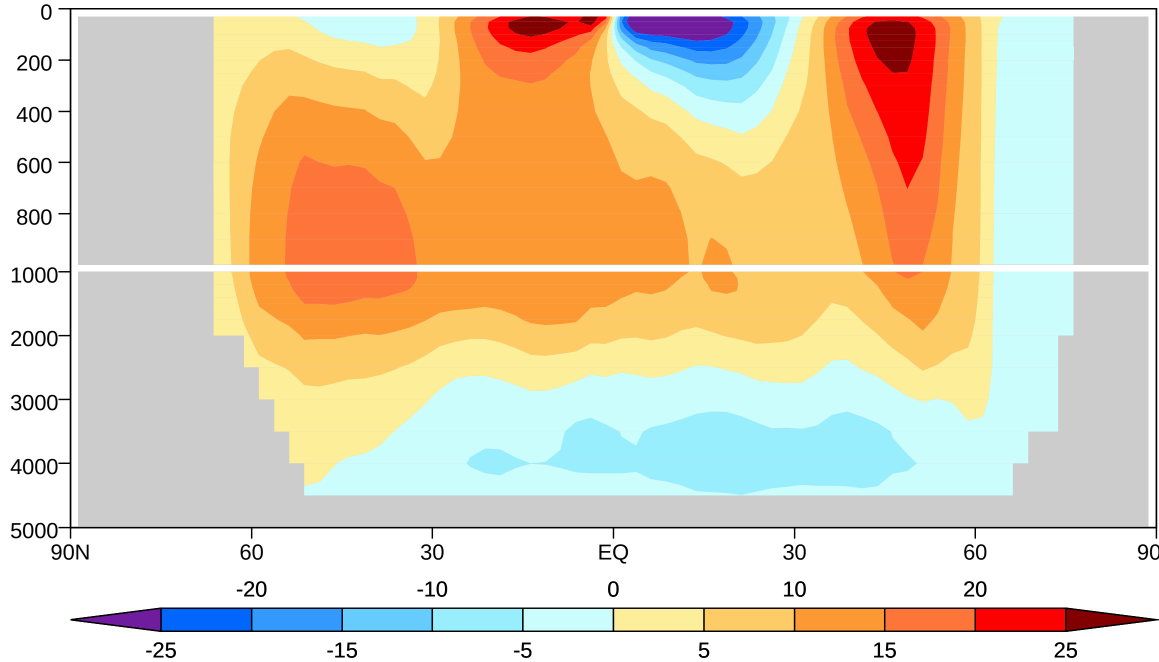

Figure 8.3.24. Zonally averaged merdional streamfunction computed across all basins (Sv). Positive values (brown colors) imply subsidence on the northern side, southward flow below, and ascending water to the south. The flow is in the opposite direction around negative values (blue colors).

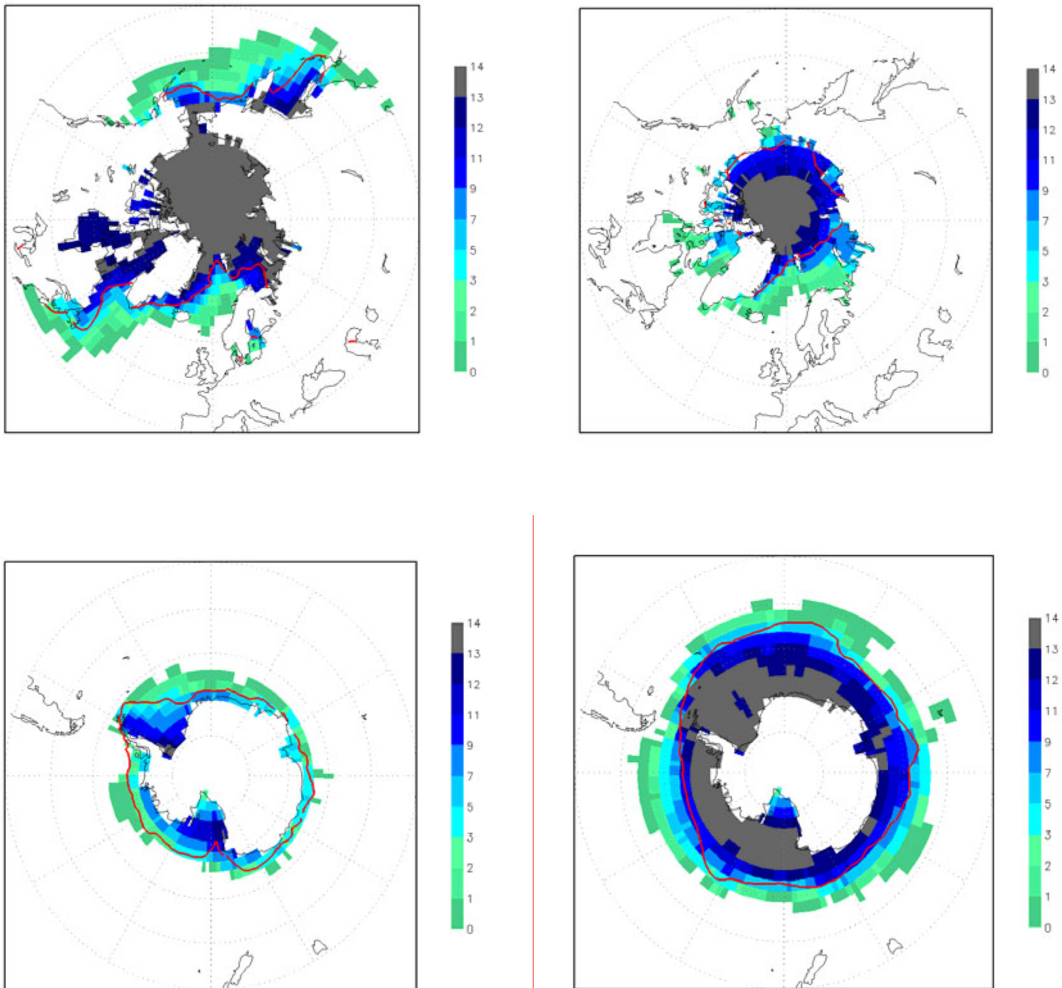

March September

Figure 8.3.25. Baseline climate (1980–1999) sea-ice distribution in the Northern (upper panels) and Southern (lower panels) Hemispheres simulated by fourteen of the AOGCMs listed in Table 8.3.1 for March (left) and September (right), adapted from Arzel et al. (2005). For each 2.5° × 2.5° longitude-latitude grid cell, the figure indicates the number of models that have at least 15% of the area covered by sea ice. The observed 15%-concentration boundaries (red line) are based on HadISST (Rayner et al., 2003).

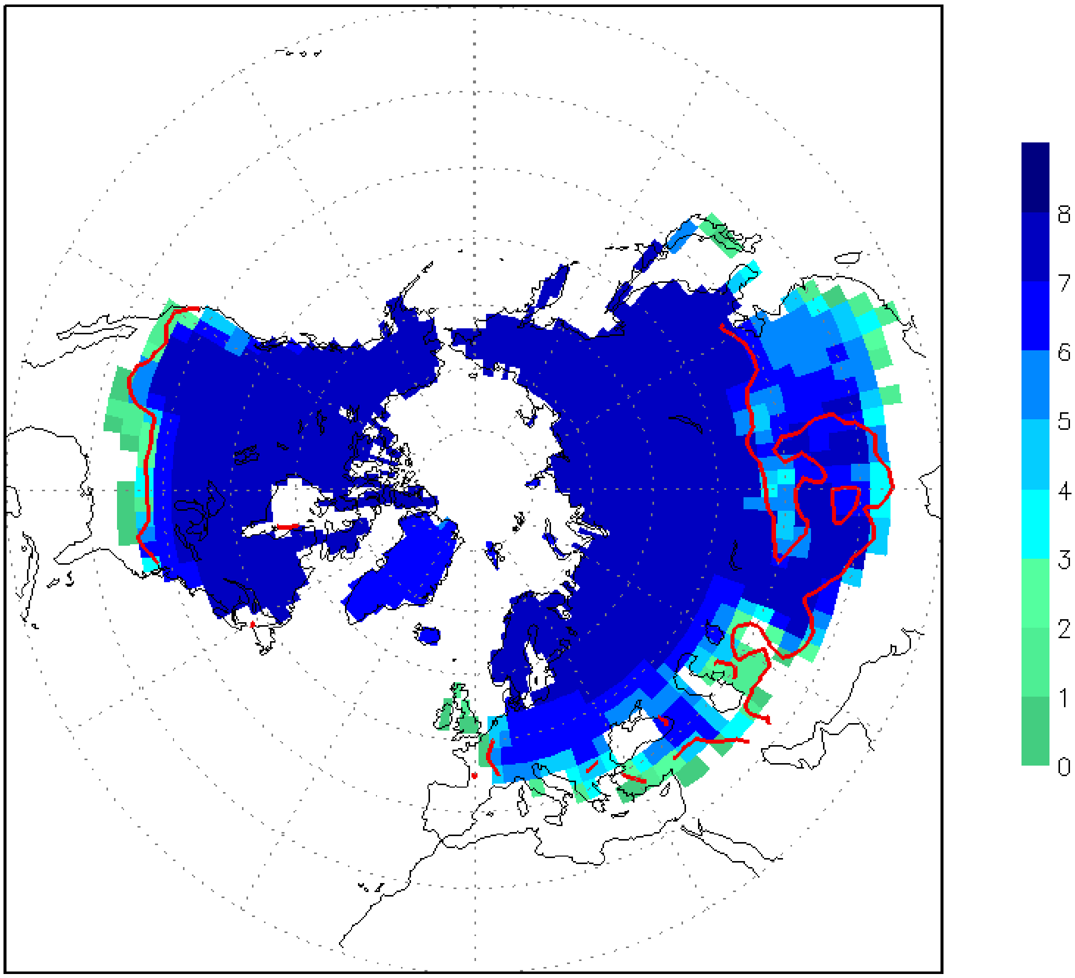

Figure 8.3.26. Baseline climate (1980–1999) terrestrial snow cover distribution in February in the Northern Hemisphere simulated by eight of the AOGCMs listed in Table 8.3.1. For each 2.5° × 2.5° longitude-latitude grid cell, the figure indicates the number of models that have at least 2.5 cm depth of snow cover. The observed 20% area coverage boundaries (red line) are based on observational data available from http://climate.rutgers.edu/snowcover (Robinson and Frei, 2000; Robinson et al., 1993) and averaged over the same time period.

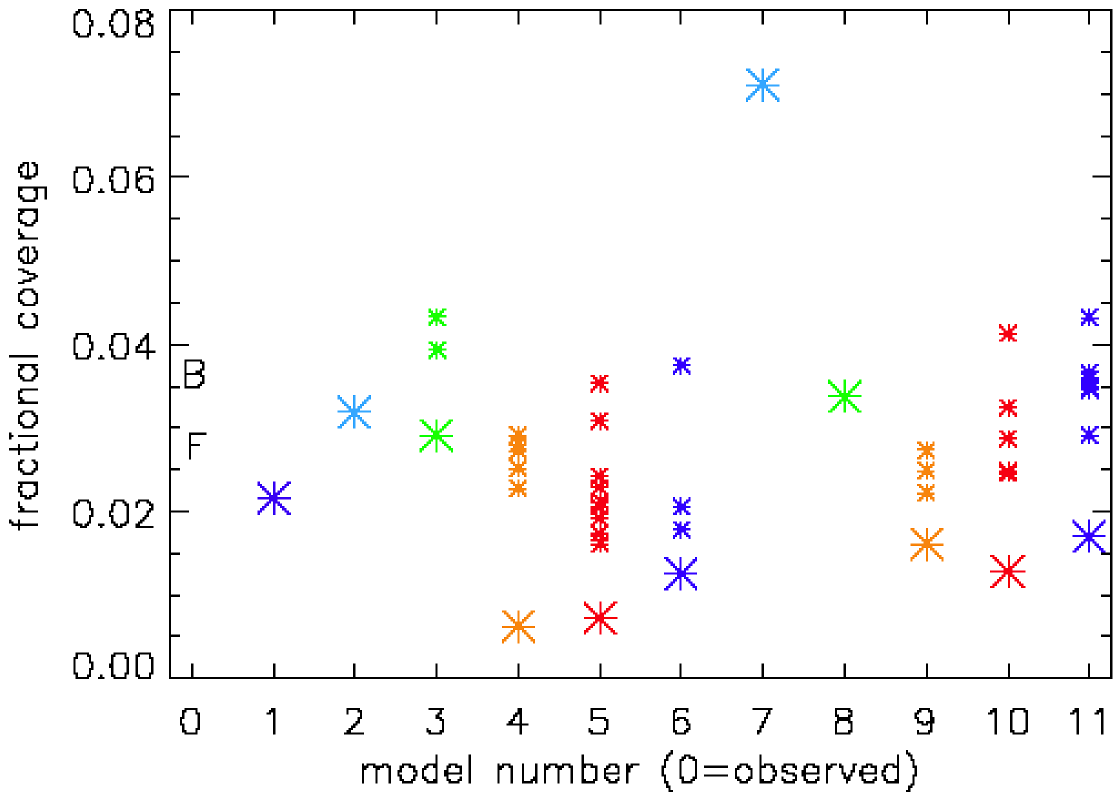

Figure 8.3.27. Decadal scale variability (DSV) of observed and modeled North American snow covered area (SCA) based on time series from 11 AOGCMs. DSV is defined as the range (maximum-minimum) of values in the detrended nine-year running mean time series of January NA-SCA for the years 1919–1993. Model number zero shows observed values: B=Brown (2000), F=Frei et al. (1999) are historical reconstructions based on station observations. For each model, the large symbol is the DSV for the ensemble mean. For models with >1 ensemble member, individual ensemble members are shown using smaller symbols. See text for further explanation. Adapted from Frei and Gong (2005).

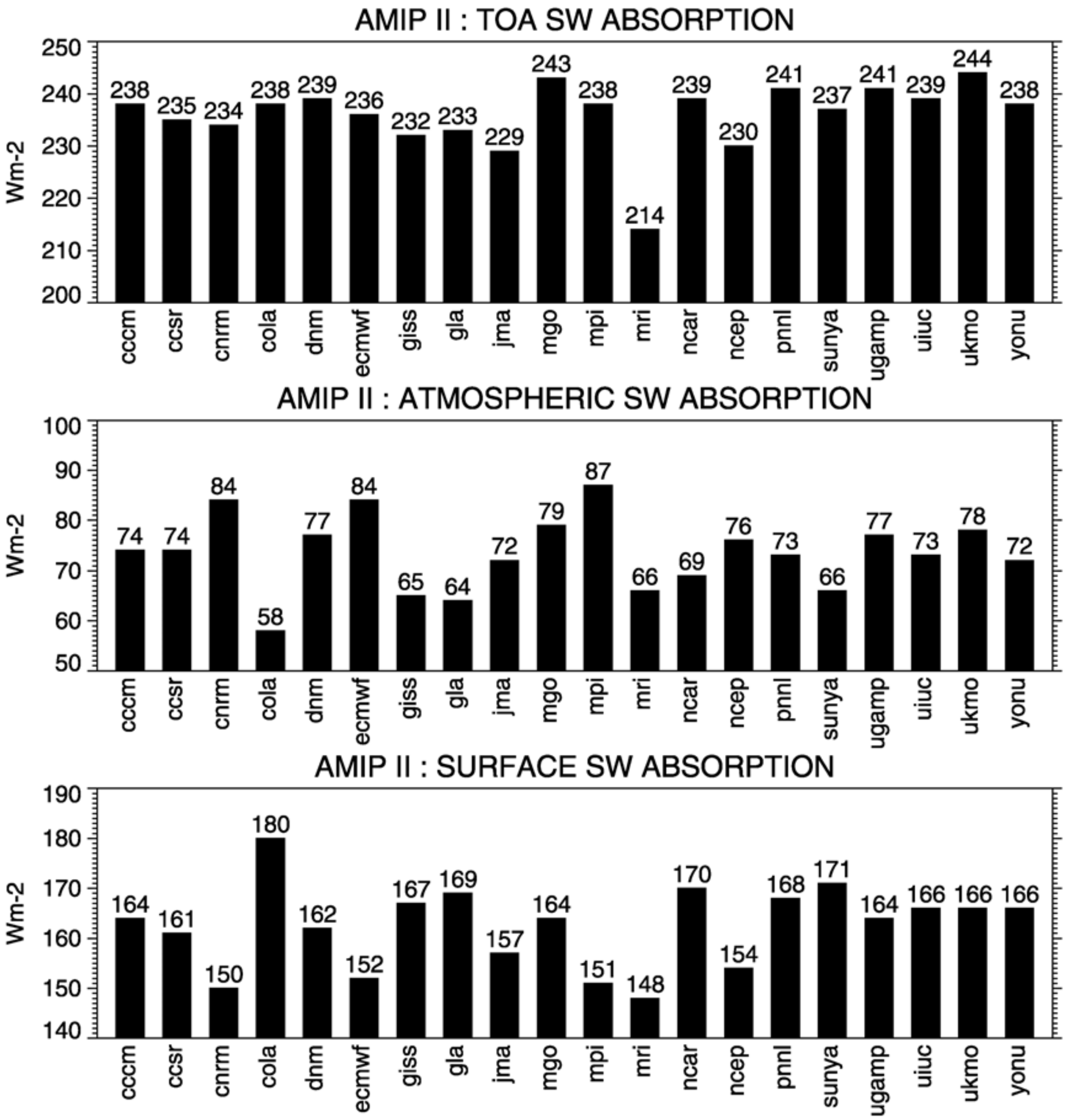

Figure 8.3.28. Global annual mean solar radiation budgets at the surface, in the atmosphere and at the TOA in 20 GCMs participating in AMIPII.

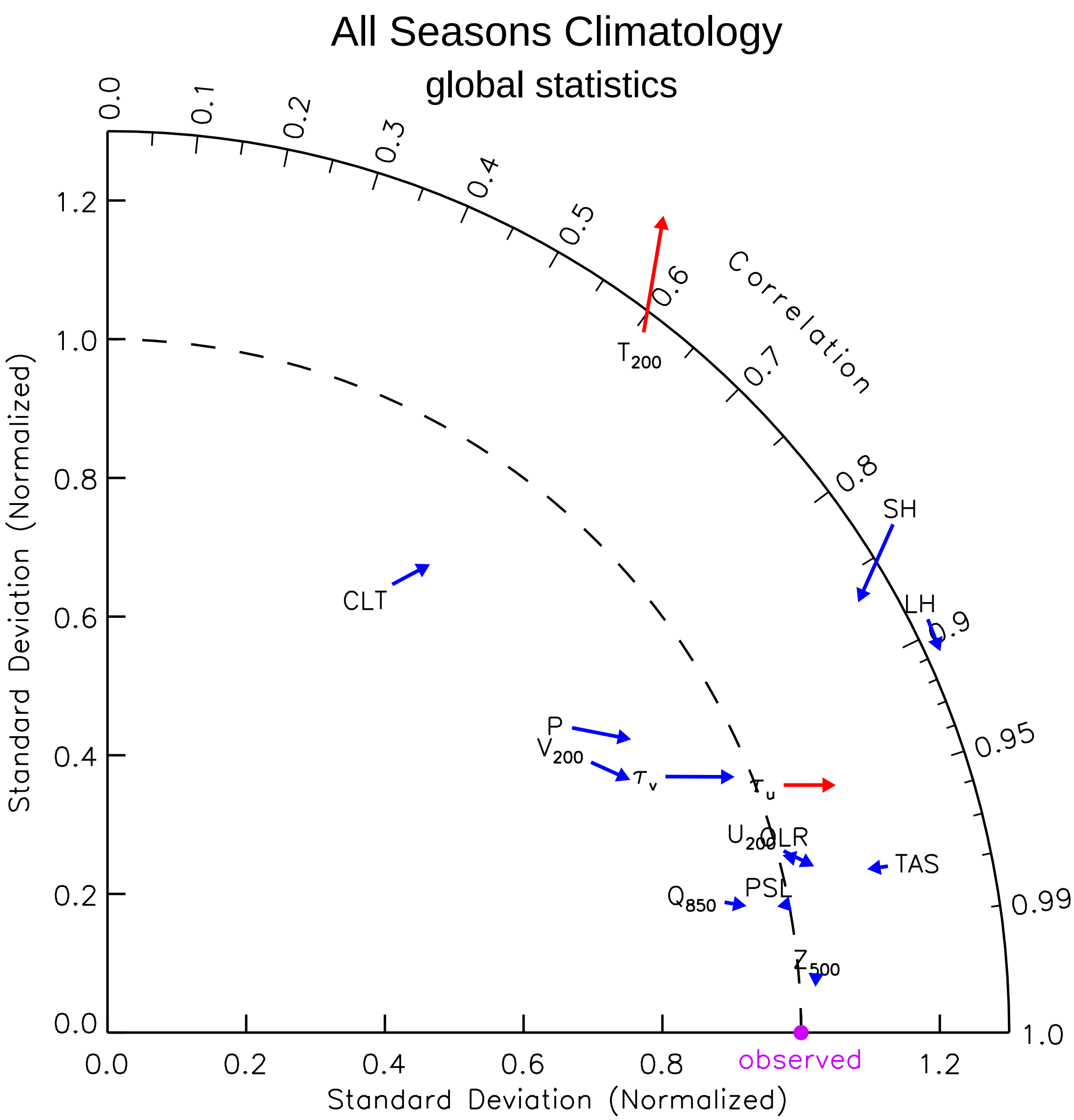

Figure 8.3.29. Changes in statistics characterizing AMIP model performance, based on the composite multi-model median fields (see text for further description). The fields analyzed were: 500 hPa geopotential height (Z_{500}), 200 hPa zonal and meridional wind (U_{200} and V_{200}), zonal and meridional components of surface wind stress over the oceans (τ_u and τ_v), mean sea level pressure over the oceans, (PSL), precipitation (P), cloud fraction (CLT), outgoing longwave radiation (OLR), 200 hPa temperature (T_{200}), 860 hPa specific humidity (Q_{850}), surface air temperature over land, and surface sensible and latent heat flux (SH and LH). Simulated fields were compared to ERA-15 (Gibson et al., 1997), with the following exceptions: precipitation was compared to CPC (Xie and Arkin, 1997), cloud fraction was compared to ISCCP (Shiffer and Rossow, 1985), OLR was compared to ERBE (Barkstrom et al., 1989), TAS was compared to CRU (Jones, 1999), and SH, LH, τ_u, and τ_v were compared to the SOC Atlas climatology (Josey et al., 1998).

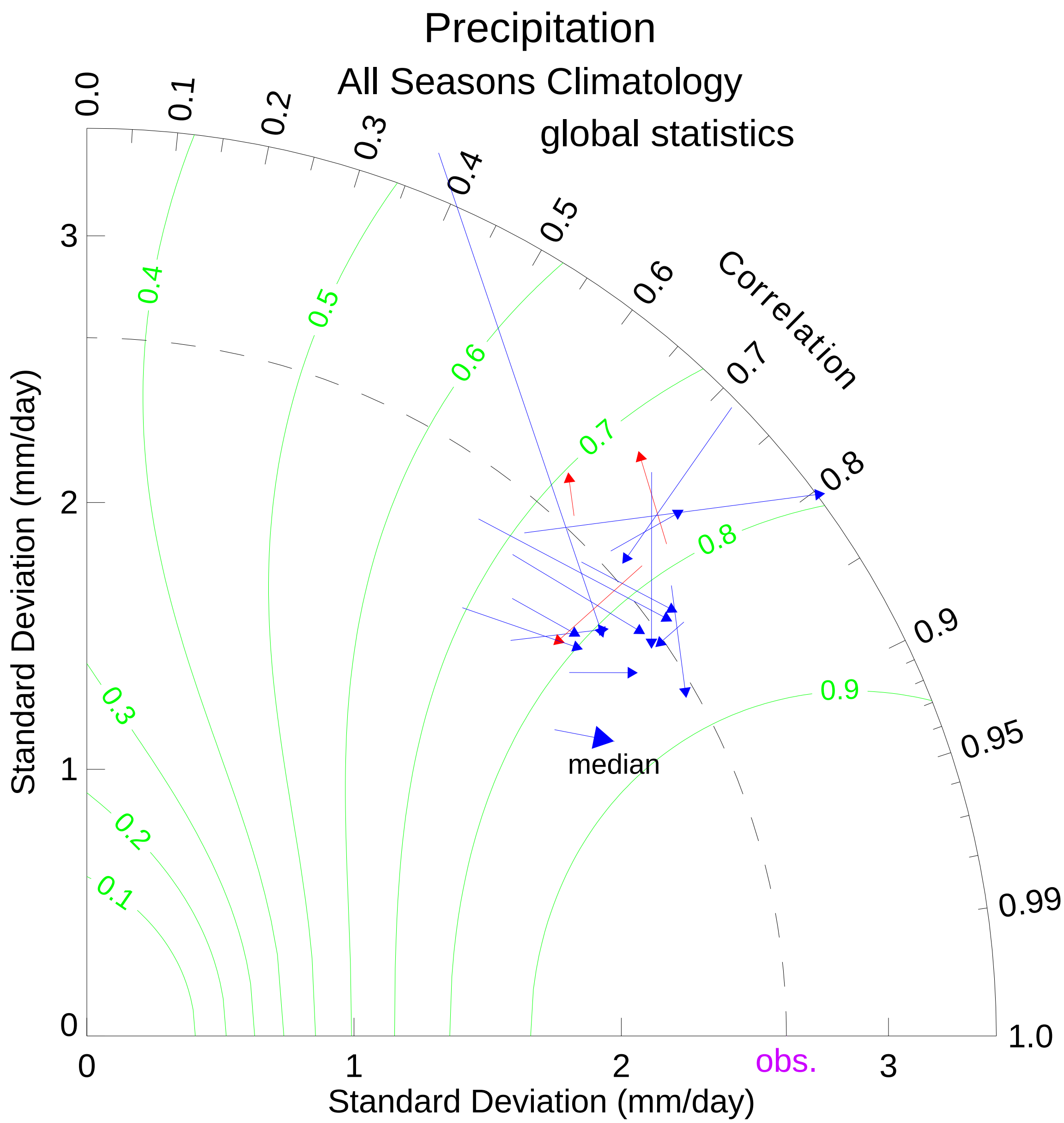

Figure 8.3.30. Changes in precipitation statistics for nineteen individual models (and the composite median field derived from the multi-model ensemble). The statistics are the same as those in Figure 8.3.29 and are defined in the text. The observations are from Xie and Arkin (1997).

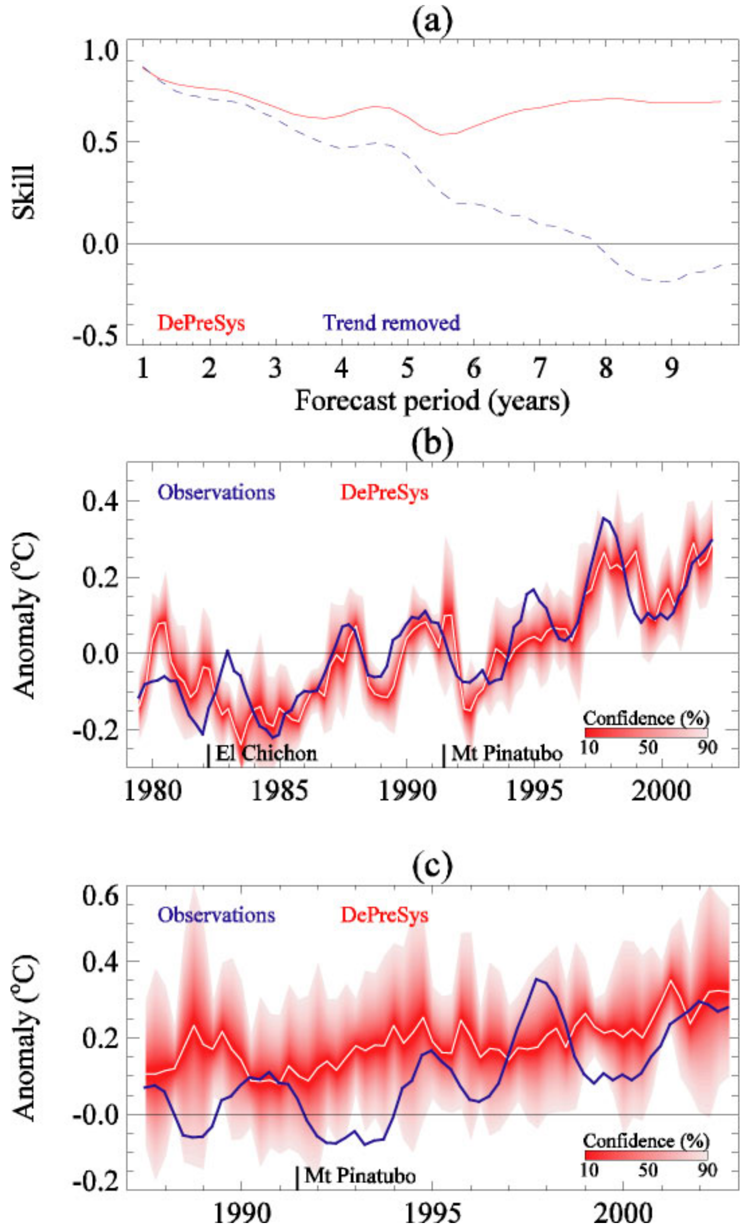

Figure 8.4.1. Hindcasts of globally averaged annual mean surface temperature, obtained from ensembles of HadCM3 simulations started from analyses of observed ocean and atmosphere anomalies and including anthropogenic and natural forcings (major volcanic eruptions are assumed not to be known about in advance). Simulations were started from 1st March, June, September and December from 1979 to 2001, with three additional ensemble members started from consecutive days preceding each start date. These four simulations were combined with the four simulations started a season earlier to form eight member ensembles. Panel (a) shows hindcast skill as a function of lead time, where skill (S) is defined as one minus the normalised error variance between hindcast and observed anomalies. S = 1 for a perfect hindcast and zero for a hindcast no better than one of zero anomaly. The dashed curve shows the component of skill attributable to internal climate variations, estimated by removing the mean global warming trend from the hindcasts. Panels (b) and (c) show time series of hindcast and observed values for hindcasts one and nine years ahead respectively. The red shading shows the hindcast confidence interval diagnosed from the ensemble standard deviation assuming a t-distribution centred on the ensemble mean (white curve).

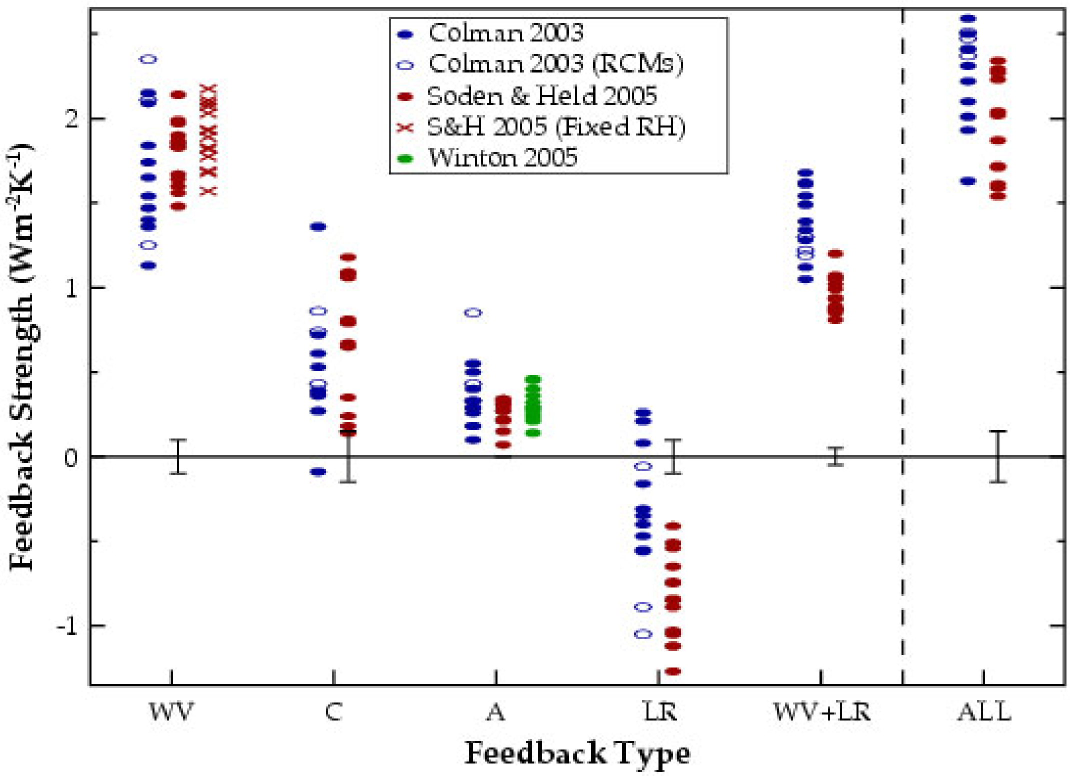

Figure 8.6.1. Comparison of GCM climate feedback parameters for water vapour (WV), cloud (C), surface albedo (A), lapse rate (LR) and the combined water vapour + lapse rate (WV+LR) in units of W m^{-2}K^{-1}. 'ALL' represents the sum of all feedbacks. Results are taken from Colman (2003) (blue), Soden and Held (2005) (red) and Winton (2005) (green). Closed and open symbols from Colman (2003) represent calculations determined using the PRP and the RCM approaches respectively. Crosses represent the water vapour feedback computed for each model from Soden and Held (2005) assuming no change in RH. Vertical bars depict the estimated uncertainty in the calculation of the feedbacks from Soden and Held (2005).

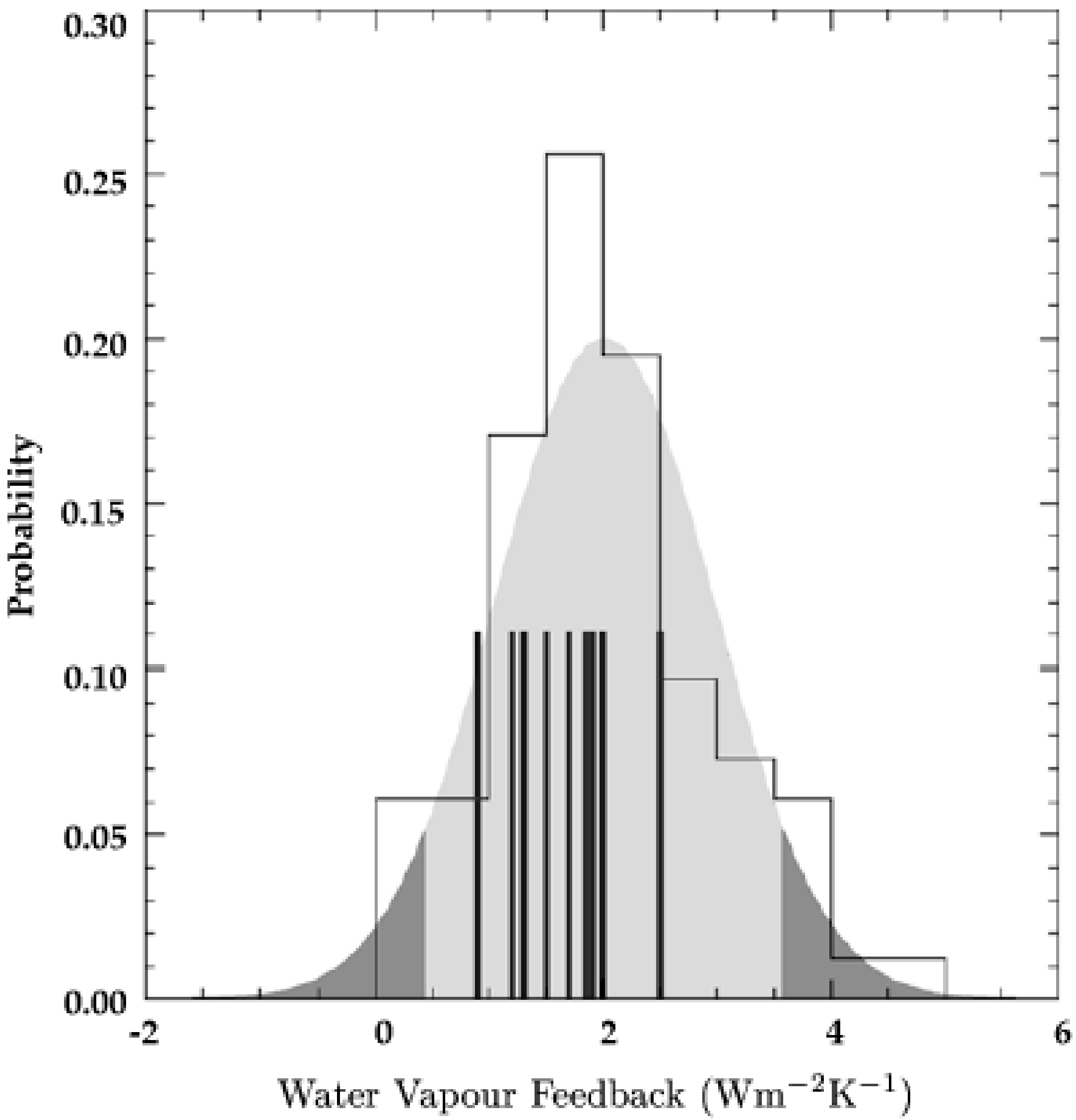

Figure 8.6.2. Estimates of water vapour feedback from the cooling associated with Mt Pinatubo, derived from observations and from an ensemble of experiments using HadCM3. The histogram denotes 82 monthly model estimates, shown in terms of probabilities. The shaded curve is a fitted normal distribution to model estimates with the 5% and 95% represented by darker shading. Observed monthly estimates are indicated by the vertical lines. (From Forster and Collins, 2004)

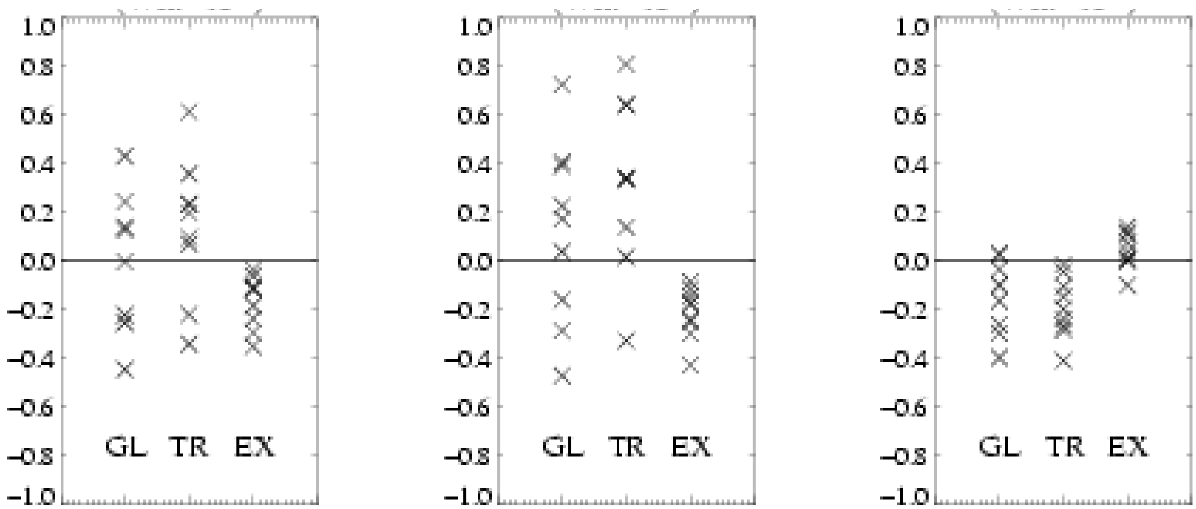

Figure 8.6.3. Change in the NET (left panel), SW (middle panel) and LW (right panel) CRF normalized by the change in global mean surface air temperature predicted by AR4 mixed-layer ocean atmosphere models in 2 × CO_2 equilibrium experiments. For each panel, results (in W $m^{-2}K^{-1}$) are shown for global (GL), tropical (30S–30N, TR) and extratropical (EX) areas. The intermodel spread of the CRF response to climate warming primarily arises from different model predictions of the change in tropical SW CRF. Adapted from Webb et al. (2005).

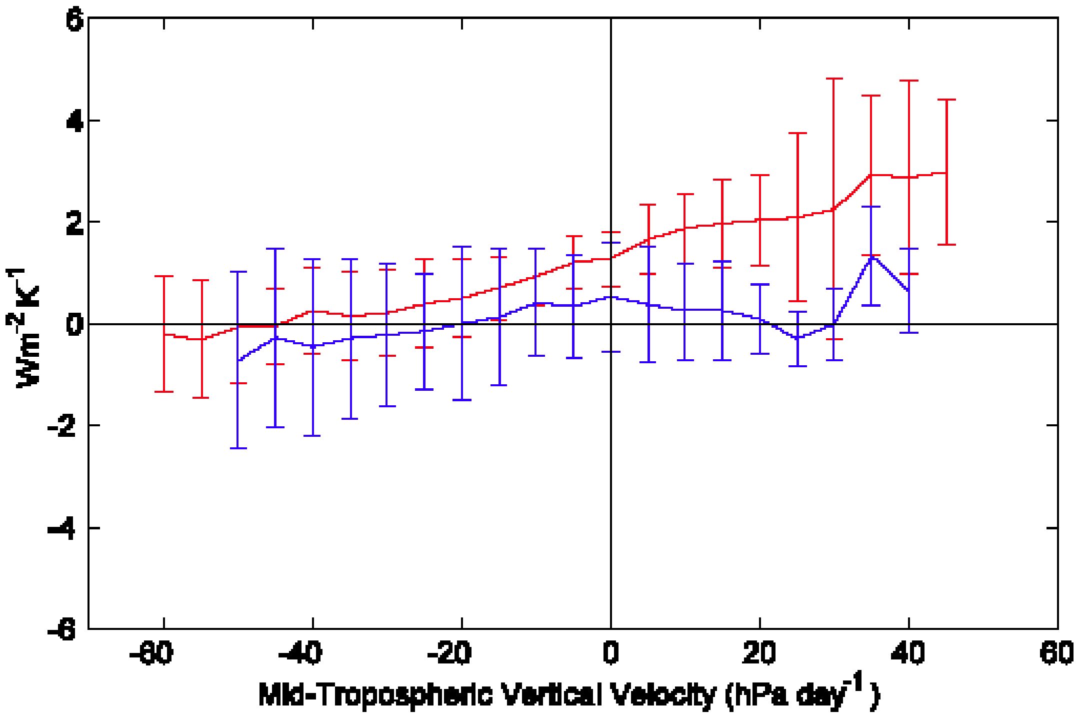

Figure 8.6.4 Sensitivity (in W $m^{-2}K^{-1}$) of the tropical SW cloud radiative forcing to sea surface temperature changes associated with climate change (in 1% per year CO2 increase experiments), derived from 15 AR4 ocean-atmosphere models in different regimes of the large-scale tropical circulation (the 500 hPa vertical pressure velocity is used as a proxy for large-scale motions, negative values corresponding to large-scale ascending motion, and positive values to large-scale subsidence). Results are presented for two groups of models: models that predict a positive anomaly of the tropical NET CRF in climate change (in red, 8 models) and models that predict a negative anomaly of the tropical NET CRF (in blue, 7 models). The large intermodel spread of the tropical CRF response to climate change primarily arises from different predictions of the radiative response of boundary-layer clouds in regimes of large-scale subsidence. From Bony and Dufresne (2005).

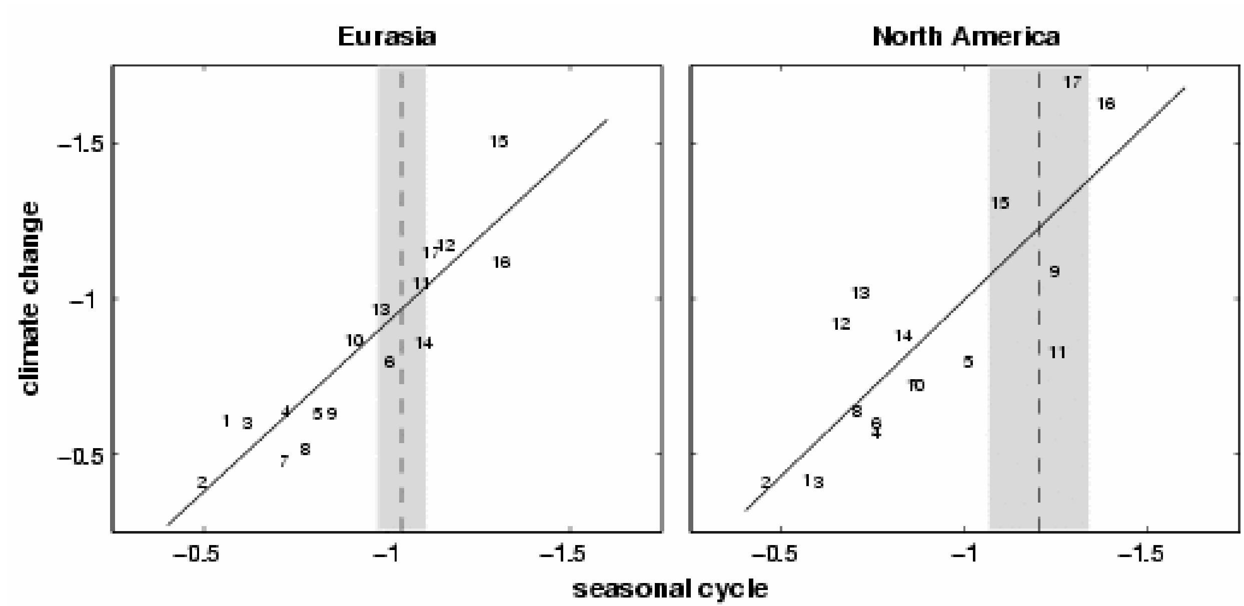

Figure 8.6.5. Scatterplots based on AR4 model output of the simulated springtime snow albedo feedback parameter in the context of external forcing (ordinate) vs. the springtime snow albedo feedback parameter in the context of the seasonal cycle (abscissa) for the Eurasian (left) and North American (right) land masses. The external forcing snow albedo feedback parameter is calculated by dividing the difference in mean April surface albedo averaged over the continents poleward of 30°N between the 22nd and 20th centuries by the difference in mean April surface air temperature between the 22nd and 20th centuries averaged over the same regions. The seasonal cycle snow albedo feedback parameter, based on 20th century climatological means, is calculated by dividing the difference between April and May northern hemisphere continental-mean surface albedos between April and May surface air temperature averaged over the same area. A least-squares fit regression line for the simulations is also shown. The seasonal cycle feedback parameter was also calculated based on the surface albedo climatology of the 1984–2000 ISCCP data set and the surface air temperature climatology of the ERA40 reanalysis from the same time period. This value is plotted as a vertical line, with the associated shaded region indicating the 95% confidence interval of the estimate due to the shortness of the time series. Numbers, used as plotting symbols, correspond to the following AR4 transient climate change experiments: (1) cnrm_cm3, (2) mri_cgcm2_3_2a, (3) giss_model_e_r, (4) csiro_mk3_0, (5) ncar_pcm1, (6) ukmo_hadcm3, (7) cccma_cgcm3_1, (8) iap_fgoals1_0_g, (9) mpi_echam5, (10) ukmo_hadgem1, (11) miub_echo_g, (12) ipsl_cm4, (13) ncar_ccsm3.0, (14) miroc3_2_medres, (15) inmcm3.0, (16) gfdl_cm2_0, (17) gfdl_cm2_1. The Northern Hemisphere snow albedo feedback's magnitude in the context of the present-day climatological springtime rise in temperatures is highly correlated with its magnitude in the context of centennial-scale human-induced climate change. Therefore if the strength of snow albedo feedback in the present-day seasonal cycle is known for any particular model, its strength in the climate change context can be accurately predicted. Since the real world's seasonal cycle is well-sampled, the strength of snow albedo feedback in the context of the real seasonal cycle is easily measured and compared to the simulated values. Adapted from Hall and Qu (2005).

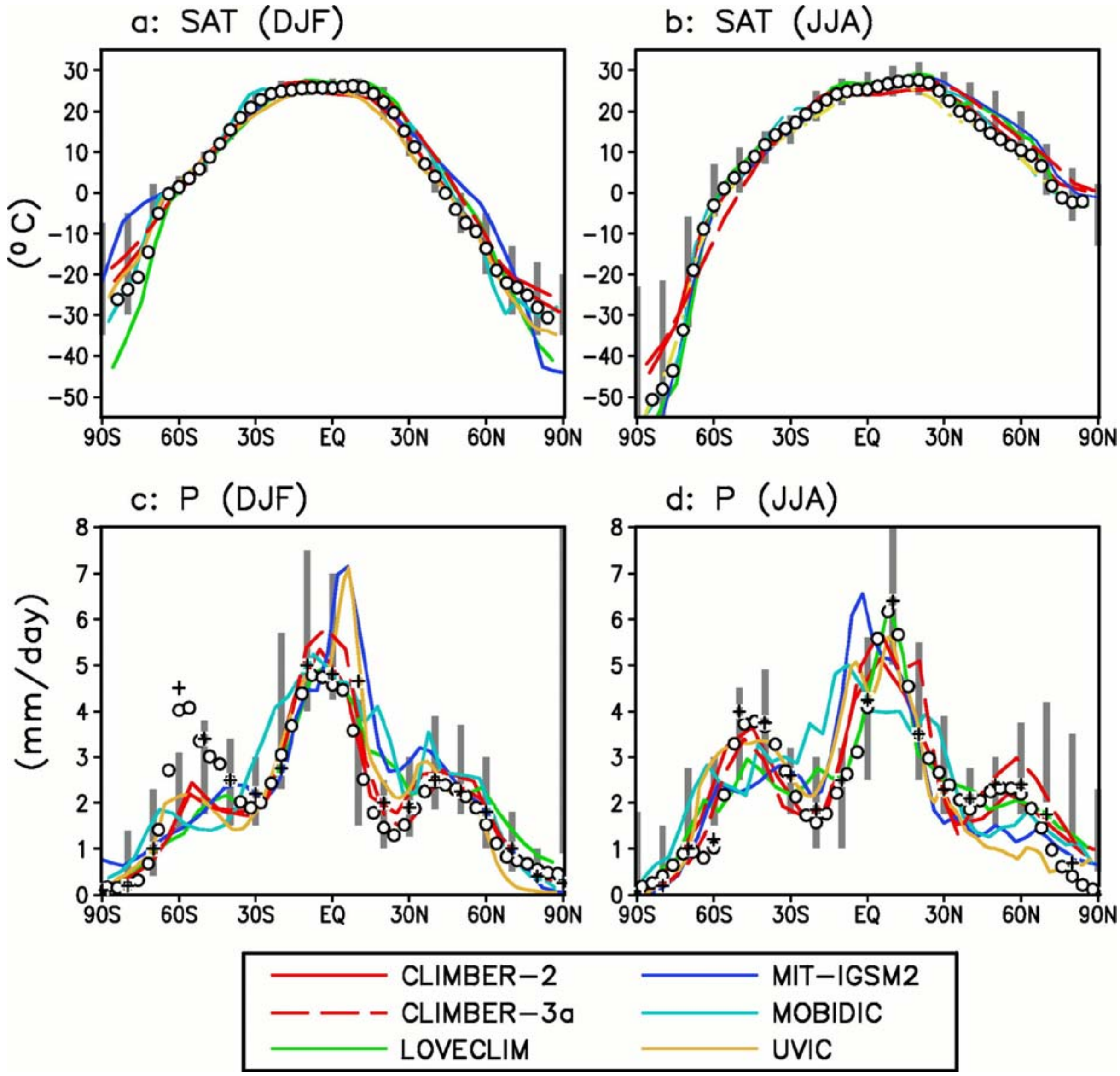

Figure 8.8.1. Latitudinal distributions of the zonally averaged surface temperature (a, b) and precipitation (c,d) for present-day boreal winter (December, January, February; DJF) (a,c) and boreal summer (June, July, August; JJA) (b,d) as simulated by some of the EMICs used in Chapter 10 of the present report (see Table 8.8.2). Observational data are represented by circles and crosses. The vertical gray bars indicate the range of GCM results (see text). Note that the version of LOVECLIM employed in this intercomparison exercise has no biosphere and inland ice components. The version of MIT-IGSM2 also somewhat differs from the one described in Table 8.8.2. (Adapted from Petoukhov et al., 2005).

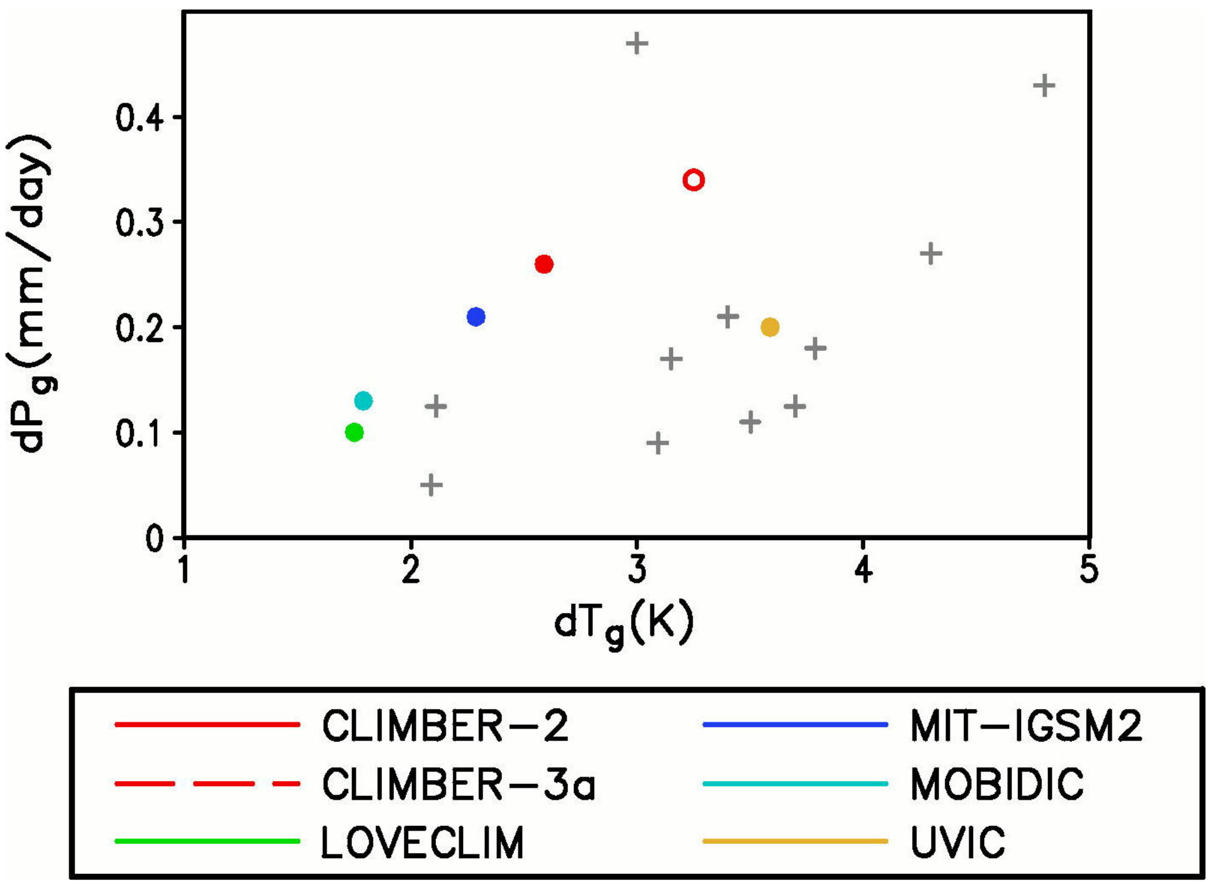

Figure 8.8.2. Differences in globally averaged, annual mean surface temperature (dT_g) and precipitation (dP_g) between an equilibrium climate adjusted to a doubling of atmospheric CO_2 concentration and the pre-industrial climate. The coloured dots refer to results obtained by some of the EMICS used in Chapter 10 of the present report (Table 8.8.2), while the grey crosses correspond to results from GCMs published in Le Treut and McAveney (2000). The CLIMBER-2 and CLIMBER-3α results are represented by closed and open red circles, respectively. Note that the version of LOVECLIM utilised in this intercomparison exercise has no biosphere and inland ice components. The version of MIT-IGSM2 also somewhat differs from the one described in Table 8.8.2. (Adapted from Pethoukhov et al., 2005.)

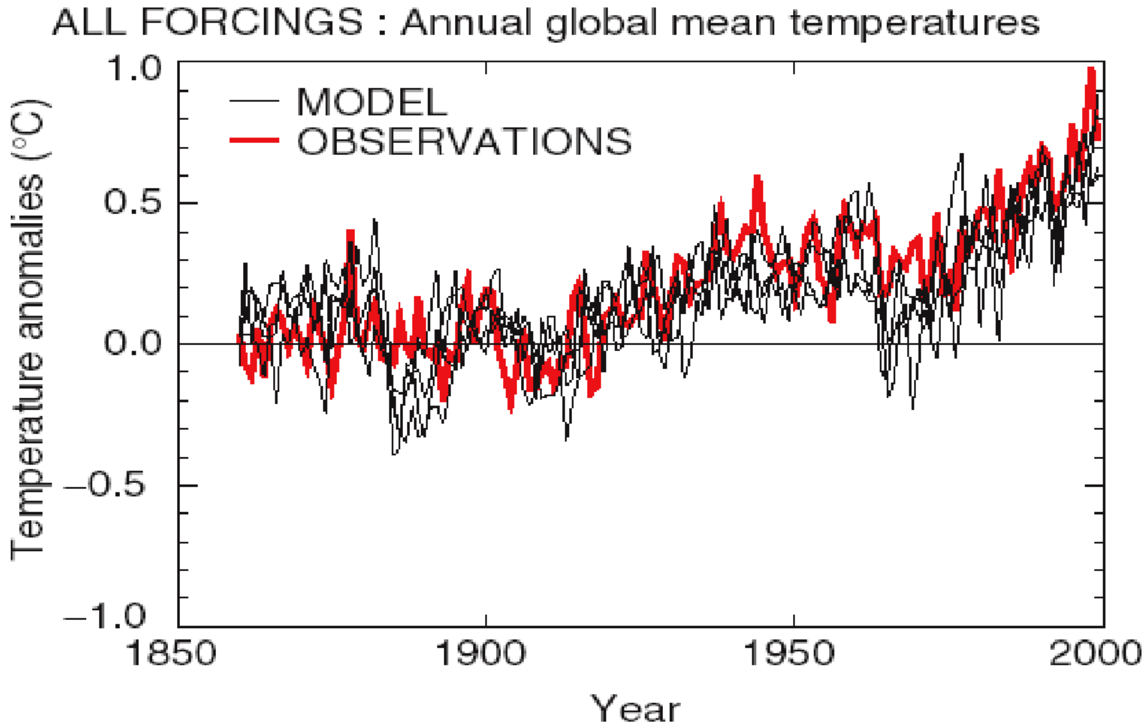

Question 8.1, Figure 1. Globally averaged surface air temperature, from observations, and as simulated by climate models for the instrumental record climate in response to major forcings, natural and anthropogenic. The multiple model lines represent an ensemble of model runs, which together indicate that internal (unforced) variability is unlikely to be a good explanation for the trends simulated (Source: IPCC, 2001).